

Frequency-Encoded Deep Learning with Speed-of-Light Dominated Latency

Ronald Davis III¹, Zaijun Chen^{1,3}, Ryan Hamerly^{1,2}, and Dirk Englund¹

¹Research Laboratory of Electronics, MIT, Cambridge, MA, 02139, USA

²NTT Research Inc., PHI Laboratories, 940 Stewart Drive, Sunnyvale, CA 94085, USA and

³Ming Hsieh Department of Electrical and Computer Engineering,
University of Southern California, Los Angeles, California 90089, USA

The ability of deep neural networks to perform complex tasks more accurately than manually-crafted solutions has created a substantial demand for more complex models processing larger amounts of data. However, the traditional computing architecture has reached a bottleneck in processing performance due to data movement from memory to computing. Considerable efforts have been made towards custom hardware acceleration, among which are optical neural networks (ONNs). These excel at energy efficient linear operations but struggle with scalability and the integration of linear and nonlinear functions. Here, we introduce our multiplicative analog frequency transform optical neural network (MAFT-ONN) that encodes the data in the frequency domain to compute matrix-vector products in a single-shot using a single photoelectric multiplication, and then implements the nonlinear activation for all neurons using a single electro-optic modulator. We experimentally demonstrate a 3-layer DNN with our architecture using a simple hardware setup assembled with commercial components. Additionally, this is the first DNN hardware accelerator suitable for analog inference of temporal waveforms like voice or radio signals, achieving bandwidth-limited throughput and speed-of-light limited latency. Our results demonstrate a highly scalable ONN with a straightforward path to surpassing the current computing bottleneck, in addition to enabling new possibilities for high-performance analog deep learning of temporal waveforms.

INTRODUCTION

DNNs are revolutionizing computing and signal processing in applications ranging from image classification and autonomous robotics to life science [1–4]. However, exponentially increasing DNN parameters over the last 20 years [5] and the large quantities of data are stretching the limits of present-day conventional computing architectures, primarily due to the “von Neumann” bottleneck in data movement from memory to processing [6]. Numerous approaches are looking to address this bottleneck by different computing paradigms like the Google Tensor Processing Unit (TPU), SRAM, DRAM, and memristor architectures that increase throughput by merging together the memory operations and matrix computations into single hardware elements [6].

Optical systems promise DNN acceleration by encoding, routing, and processing analog signals in optical fields, allowing for operation at the quantum-noise-limit with high bandwidth and low energy consumption. Optical neural network (ONN) schemes rely on (i) performing linear algebra intrinsically in the physics of optical components and/or (ii) in-line nonlinear transformations $f(\cdot)$. For (i), past approaches include Mach-Zehnder interferometer (MZI) meshes [7–10], on-chip micro-ring resonators (MRRs) [11–14], wavelength-division multiplexing (WDM) [15–17], photoelectric multiplication [18], spatial light modulation [19–24], optical scattering [25], and optical attenuation [26]. For (ii), past approaches include optical-electrical-optical (OEO) elements [26–29] and all-optical [13, 23, 30–33] approaches. However, to fully take advantage of the potential ultra-low latency and energy consumption available in photonics, it is necessary to implement *linear and nonlinear operations* together with minimal overhead. Simultaneously achieving (i) and (ii) in a way that preserves high hardware scalability and performance has

been an open challenge.

Our multiplicative analog frequency transform optical neural network (MAFT-ONN) architecture simultaneously achieves (i) and (ii) for DNN inference with arbitrary scalability in DNN size and layer depth. We experimentally demonstrate the MAFT-ONN in a 3-layer DNN for inference of MNIST images. In this architecture, we encode neuron values in the amplitude and phase of frequency modes, and ‘photoelectric multiplication’ [18] performs matrix-vector products in a single shot. In a proof-of-concept experiment with commercial components, we realize the MAFT-ONN scheme that combines efficient optical matrix operations with in-line nonlinear transformations by electro-optic nonlinearities, enabling a scalable front-to-back photonic hardware accelerator for DNNs. This architecture enables DNN inference for an arbitrary number of layers using a simple hardware setup that maintains high throughput and ultra-low latency, which are important performance metrics for applications like voice recognition, spectral channel monitoring, distributed sensing, and cognitive radio. Figure 1(a) contextualizes use-cases for the MAFT-ONN processor.

MAFT-ONN ARCHITECTURE

As illustrated in Figure 1(b), a generic DNN consists of an input layer, at least one hidden layer, and an output layer that yields the processed data. As seen in Figure 1(c), these DNN layers map to a series of photonic hardware layers, indexed here from $j = 1 \dots J$. Figure 1(d) details an arbitrary layer j with N input and R output neurons. Thus, the input vector $X^{(j)}$ has size $N \times 1$, the weight matrix $W^{(j)}$ has size $R \times N$, and the output vector $Y^{(j)} = W^{(j)}X^{(j)}$ has size $R \times 1$.

Matrix algebra: The values of $X^{(j)}$, $W^{(j)}$, and $Y^{(j)}$ are

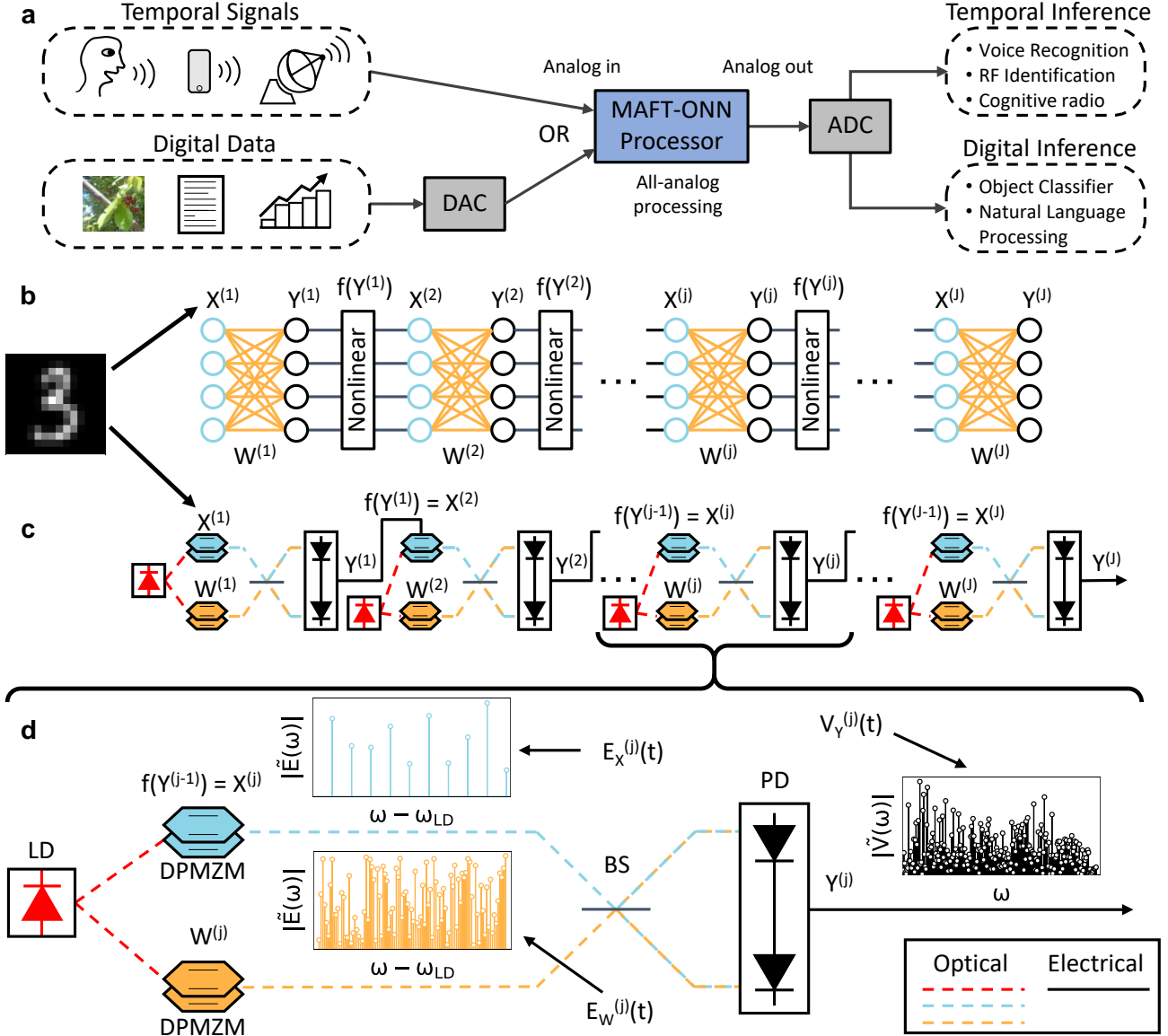


Figure 1. An overview of the MAFT-ONN architecture. (a) The MAFT-ONN is suitable to directly process analog temporal signals like voice and RF waveforms, and also processes digital data using a digital-to-analog converter (DAC). The analog output of the MAFT-ONN is read out digitally using an analog-to-digital converter (ADC). (b) A typical, arbitrarily long DNN, where each layer consists of a matrix-vector multiplication and a nonlinear activation. (c) An outline of the MAFT-ONN architecture, where both the inputs and weights are encoded in the frequency domain and then modulated onto optical carriers. The photoelectric multiplication yields the linear matrix-vector product for each layer, while each DPMZM provides the nonlinear activation. (d) A close-up of a single layer. The DPMZM of the current layer j acts as the nonlinear activation function for the previous layer $j - 1$. The weight matrix signal is programmed to yield the matrix-vector product while simultaneously transforming the input vector frequencies into a chosen set of output vector frequencies.

all contained in frequency-encoded signals. The input vector to layer j , $X^{(j)}$, begins as an optical field $E_X^{(j)}(t)$, which is the result of modulating a laser diode (labeled LD) via a dual-parallel Mach-Zehnder modulator (DPMZM) that is driven by the photovoltage output of the previous layer $j - 1$. Let the neuron values of $X^{(j)}$ have a frequency spacing $\Delta\omega_X$ and offset $n_0 \cdot \Delta\omega_X$. Then the frequency encoded signal for $X^{(j)}$ is:

$$E_X^{(j)}(t) \propto \sum_{n=1}^N X_n^{(j)} e^{i(n_0+n)\Delta\omega_X + \omega_{LD}t},$$

where ω_{LD} is the laser frequency.

The weight matrix $W^{(j)}$ also begins as an electrical signal, $V_W^{(j)}(t)$. We choose to encode $V_W^{(j)}(t)$ so that the output vector $Y^{(j)}$ has frequency spacing $\Delta\omega_Y$ and offset $r_0 \cdot \Delta\omega_Y$. After modulating $V_W^{(j)}(t)$ on a DPMZM, the

weight matrix optical field is:

$$E_W^{(j)}(t) \propto \sum_{r=1}^R \sum_{n=1}^N W_{r,n}^{(j)} e^{i((r_0+r)\Delta\omega_Y + (n_0+n)\Delta\omega_X + \omega_{LD})t}.$$

Figure 1(d) plots the frequency content $\tilde{E}(\omega)$ of the optical input $E_X^{(j)}(t)$ and weights $E_W^{(j)}(t)$, where the tilde over a variable indicates its Fourier Transform. Note that both of these signals are single-sideband with respect to the laser carrier.

Sending $E_X^{(j)}(t)$ and $E_W^{(j)}(t)$ through a 50:50 beamsplitter (labeled BS) onto a balanced photodetection apparatus (labeled PD) produces a photovoltage

$$V_{\text{out}}^{(j)}(t) \propto \text{Im} \left[\left(E_X^{(j)}(t) \right)^* E_W^{(j)}(t) \right] \quad (1)$$

$$\propto V_Y^{(j)}(t) + V_S^{(j)}(t), \quad (2)$$

where we ignore linear scaling factors here (see the Discussion section for the link gain analysis). Here, the partial sums of $Y^{(j)}$ coherently summed in the frequency domain to yield the desired matrix product in a single shot:

$$V_Y^{(j)}(t) \propto \sum_{r=1}^R Y_r^{(j)} \sin((r_0 + r)\Delta\omega_Y t). \quad (3)$$

Thus, this MAFT scheme transforms an input signal with frequency spacing $\Delta\omega_X$ into an output signal with spacing $\Delta\omega_Y$ while simultaneously computing a matrix-vector product. The signal $V_S^{(j)}(t)$ contains ‘spurious frequencies’ that do not contribute to the matrix-vector product. In practice, we eliminate $V_S^{(j)}(t)$ using passive RF bandpass filters or RF cavities/optical ring resonators with a free-spectral range equal to $\Delta\omega_Y$. However, in DNN training, we found a benefit to retaining $V_S^{(j)}(t)$, as discussed later. For a more detailed and generalized derivation of the MAFT scheme, see Supplementary Section E. **Nonlinear activation:** We achieve the nonlinear activation $f(\cdot)$ by applying $V_Y^{(j)}(t)$ to the nonlinear regime of an MZM, yielding the optical input to the next layer $j+1$:

$$\begin{aligned} f(V_Y^{(j)}(t)) &= E_X^{(j+1)}(t) \\ &= \chi_0 + \chi_1 e^{i\omega_{LD}t} \cdot \text{H}_a \left[\sin \left(\chi_2 V_Y^{(j)}(t) + \chi_3 \right) \right]. \end{aligned} \quad (4)$$

Here, χ_0 contributes to the DC offset; χ_1 depends on the laser power, insertion loss, and propagation loss; χ_2 depends on the V_π and efficiency of the MZM; and χ_3 depends on the bias conditions and inherent bias point of the MZM. Using these four parameters, we can program the strength of the nonlinearity. The function $\text{H}_a[\cdot]$ is the analytic Hilbert transform, which removes the negative frequency components from the sinusoids (making them complex-valued) to ensure that $E_X^{(j+1)}(t)$ is single-sideband with respect to the laser carrier, as $E_X^{(j)}(t)$ and

$E_W^{(j)}(t)$ are. Therefore, the MZM simultaneously encodes the next layer’s input vector while also implementing the nonlinear transformation on $V_Y^{(j)}(t)$.

The Fourier transform of $E_X^{(j+1)}(t)$ (written in the time domain in Equation 4) reveals an unusual property of $f(\cdot)$: the nonlinearity applied to one neuron $Y_r^{(j)}$ depends on all neurons via an expression of the form $f(Y_r^{(j)}, Y_1^{(j)}, \dots, Y_R^{(j)})$. Whereas for a conventional DNN, $f(\cdot)$ acts element-wise on each vector component. We incorporated this ‘all-to-all’ nonlinearity into our training procedure (see below) for the conventional DNN tasks considered in this work, but note that other works call for such data-dependent nonlinear activations for applications like adversarial DNNs [34].

Remarks: (i) The MAFT scheme presented here readily extends to matrix-matrix multiplication via time or frequency-multiplexing of the input vector $V_X(t)$. For time-multiplexing, we append M input vectors in the time domain, which corresponds to batching several inputs to be inferred by the same weight matrix. See Supplementary Section J for more details. For frequency-multiplexing, see Figure 4(a). (ii) Note that in this analysis, all frequencies are equally spaced to maximize the throughput of the matrix-vector computations.

2 × 2 Matrix Experimental Demonstration

Figure 2 walks through an experimental example of a 2 × 2 matrix-vector multiplication using the MAFT scheme. Figure 2(a) keeps track of all the matrix and partial sum elements. The input and weight electrical voltage signals $V_X(t)$ and $V_W(t)$, respectively, were generated by an arbitrary waveform generator (AWG) and then sent to DPMZMs. These DPMZMs perform single-sideband suppressed carrier (SSB-SC) modulation of the signals, without which the modulated signals would be dual-sideband and completely cancel each other out after the photoelectric multiplication. To SSB-SC modulate an arbitrary signal, one copy of the signal is sent to one of the sub-MZMs of the DPMZM, and another 90° phase-shifted copy is sent to the other sub-MZM. Thus, let an underbar indicate an analytical Hilbert transform, yielding $\underline{V}_X(t) = \text{H}_a[V_X(t)]$. Then $\text{Re}[\underline{V}_X(t)] = V_X(t)$ is the original signal, and $\text{Im}[\underline{V}_X(t)]$ is the 90° phase-shifted copy. Figure 2 illustrates both signals in the time domain since they have the same magnitude in the frequency domain. (Although the 90° phase-shifted was generated using an AWG in this experiment, in deep neural nets this phase shift can be achieved using commercial wide-band passive RF phase shifters.)

In this example, $V_X(t)$ contains two frequencies, $V_W(t)$ contains four frequencies, and the output electrical voltage signal $V_{\text{out}}(t)$ contains a variable number of frequencies. We keep $V_X(t)$ the same while altering $V_W(t)$ to demonstrate various effects. In Figure 2(b), $V_W(t)$ is programmed so that each partial sum in $V_{\text{out}}(t)$ maps to a unique frequency, thus performing no summation in the frequency domain. In Figure 2(c), $V_W(t)$ is programmed so that the frequency domain of $V_{\text{out}}(t)$ yields a matrix-vector prod-

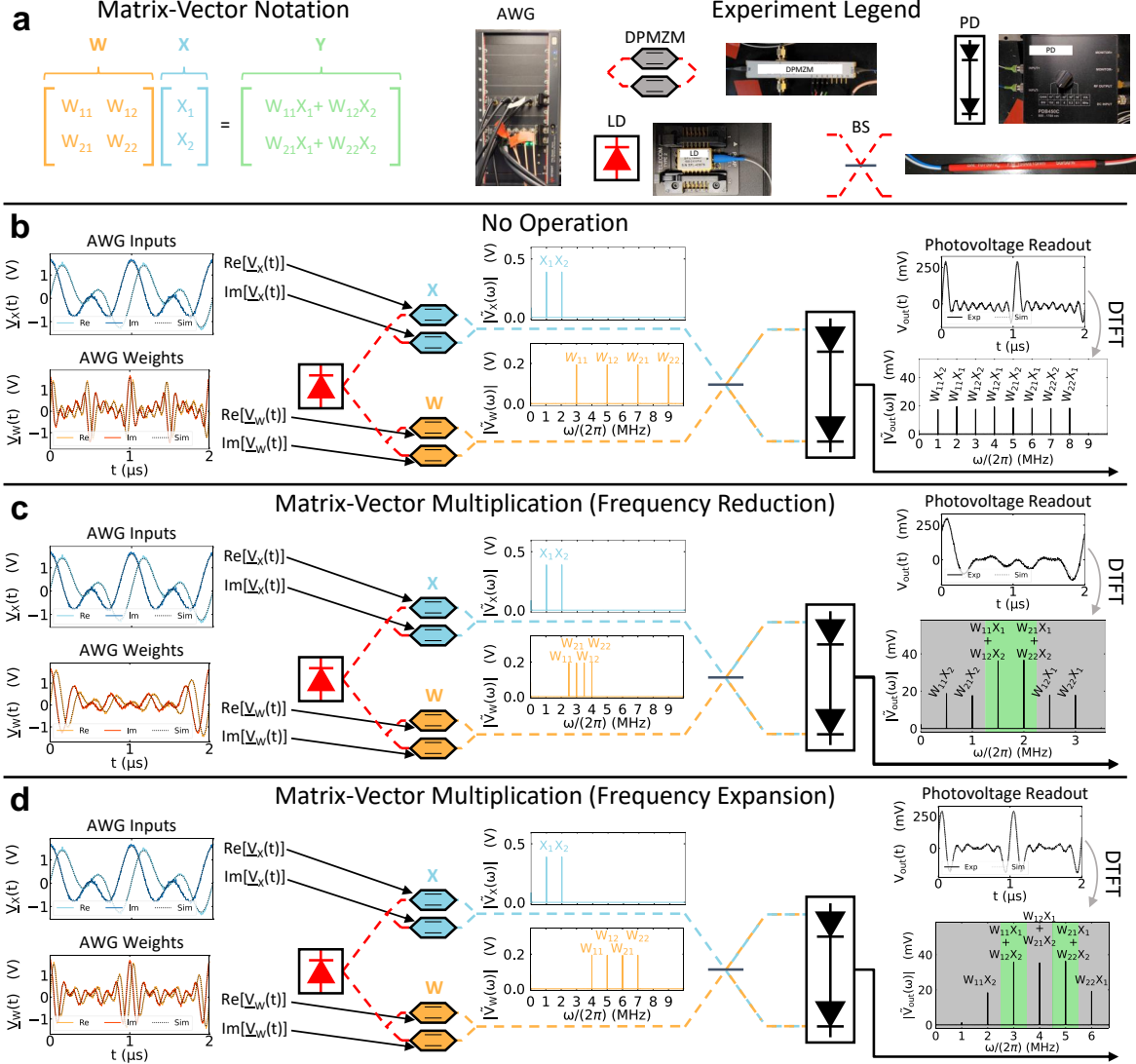


Figure 2. An experimental example of a 2×2 matrix-vector multiplication using the MAFT scheme. Each time domain plot shows one period of the raw data from the oscilloscope, and each frequency domain plot shows the discrete time Fourier transform (DTFT) of the entirety of the oscilloscope trace. (a) The notation for a typical 2×2 matrix multiplication between a matrix W and a vector X . The legend contains photos of the commercial components used to conduct the experiments in this figure. (b) No operation. In this case, the frequencies of $V_W(t)$ were chosen to demonstrate a separation of the eight partial sums contained in the frequencies of $V_{out}(t)$. Here, the spurious frequencies (gray region) are pushed to either side of the neuron frequencies. The unique partial sum terms contained in the spurious frequencies of $V_{out}(t)$ will either be removed with a bandpass filter or used to train a DNN. (c) Frequency reduction scheme. Here, $V_W(t)$ is programmed to yield a matrix-vector product where $\Delta\omega_Y < \Delta\omega_X$. The unique partial sum terms contained in the spurious frequencies of $V_{out}(t)$ will either be removed with a bandpass filter or used to train the DNN. (d) Frequency expansion scheme. Here, $V_W(t)$ is programmed so that $\Delta\omega_Y > \Delta\omega_X$. As with the previous scheme, the spurious frequencies in $V_{out}(t)$ will either be removed with a periodic filter or used to train the DNN. The two frequency encoding schemes can be used alternatively to avoid bandwidth limitations for arbitrarily deep DNNs.

uct where the frequencies corresponding to the elements of Y are adjacently spaced in the middle of the spurious frequencies. We refer to this method of programming as our *frequency reduction scheme* because $\Delta\omega_Y < \Delta\omega_X$. Figure 2(d) demonstrates an alternative method of programming $V_W(t)$, which intersperses the elements of Y with the spurious frequency components. We term this the *frequency expansion scheme*, as $\Delta\omega_Y > \Delta\omega_X$. The frequency reduction and expansion schemes can be used alternatively for consecutive layers of a DNN to avoid running out of

bandwidth. Alternatively, as demonstrated by the experiment in the next section, we can keep the spurious frequency components for training the DNN, which avoids the requirement for filters that precisely match the neuron frequencies.

Each partial sum term in $V_{out}(t)$ in Figures 2(b)-(d) can be traced to difference between the input and weight frequencies. For example, in Figure 2(b) the partial sum term $W_{22}X_1$ derives from the product of W_{22} at 9 MHz and X_1 at 1 MHz, where the difference between their frequencies

causes $W_{22}X_1$ to appear at 8 MHz.

EXPERIMENT

Experimental Apparatus

We experimentally demonstrated the MAFT-ONN scheme using the apparatus shown in Figure 3(c). An AWG generates $V_X^{(1)}(t)$, $V_W^{(1)}(t)$, and $V_W^{(2)}(t)$, all of which are modulated into the optical domain using DPMZMs. The frequency reduction scheme from Figure 2(c) was used to program $V_W^{(1)}(t)$, yielding $V_{\text{out}}^{(1)}(t)$ after the first layer. We decided to keep the spurious frequencies for DNN training, so $V_{\text{out}}^{(1)}(t) = V_Y^{(1)}(t)$. We then amplify $V_Y^{(1)}(t)$ to reach the nonlinear regime of the DPMZM in the second layer, after which it became the optical input signal $\hat{e}E_X^{(2)}(t)$ to the second layer. For convenience, we only used one sub-modulator of the DPMZM for this signal, thus modulating $V_Y^{(1)}(t)$ in the dual-sideband suppressed carrier (DSB-SC) mode. For the second layer, we programmed $V_W^{(2)}(t)$ using the frequency expansion scheme from Figure 2(d). The multiplication of the DSB-SC modulated $\hat{e}E_X^{(2)}(t)$ and the SSB-SC modulated $\hat{e}E_W^{(2)}(t)$ results in a copy of $V_{\text{out}}^{(2)}(t)$ appearing further up in the spectrum, as can be seen in the plot of $Y^{(2)}$ in Figure 3(c). Finally, the analog output of the second layer $V_{\text{out}}^{(2)}(t)$ was sampled digitally and Fourier transformed. See Supplementary Section A for more details on the 3-layer DNN experimental setup.

Linear Characterization

To test linear matrix-vector multiplication, we measure the photovoltage response $V_{\text{out}}^{(1)}(t)$ using a spectrum analyzer that scans the relevant part of the bandwidth to extract $V_Y^{(1)}(t)$. Here, the input laser is modulated by $V_X^{(1)}(t)$ and $V_W^{(1)}(t)$ via DPMZMs in the linear regime. We repeat this multiplication over randomized values of $X^{(1)}$ and $W^{(1)}$ to obtain the full set of characterization data.

To measure the accuracy of the matrix products, we use a theoretical model to compare with the experiment. From Equation 4, the result of linearly modulating the input vector is:

$$\begin{aligned} f(V_X^{(1)}(t)) &= \chi_0 + \chi_1 e^{i\omega_{LD}t} \cdot H_a \left[\sin \left(\chi_2 V_X^{(1)}(t) + \chi_3 \right) \right] \\ &\approx \chi_1 \chi_2 e^{i\omega_{LD}t} \cdot H_a \left[V_X^{(1)}(t) \right] \\ &\approx \chi_1 \chi_2 E_X^{(j)}(t) \end{aligned}$$

where we assume that $\chi_0 = \chi_3 = 0$ in the linear regime. Similarly, the linear modulation of the weight matrix yields $f(V_W^{(1)}(t)) \approx \chi_1 \chi_2 E_W^{(j)}(t)$. Therefore from Equation 1, the resulting photoelectric multiplication is:

$$\begin{aligned} V_{\text{out}}^{(1)}(t) &= \chi_{PD} \text{Im} \left[\left(\chi_1 \chi_2 E_X^{(j)}(t) \right)^* \chi_1 \chi_2 E_W^{(j)}(t) \right] \\ &= \chi_{PD} (\chi_1 \chi_2)^2 \text{Im} \left[\left(E_X^{(j)}(t) \right)^* E_W^{(j)}(t) \right], \end{aligned}$$

where χ_{PD} is determined by the responsivity of the photodetector and the termination resistance.

Hence for the linear characterization, we use a 1-parameter curve fit where the parameter estimates the value of $\chi_{PD} (\chi_1 \chi_2)^2$. To attain the curve fit parameter, we used a single randomized matrix-vector product and gradually increased the amplitude to create a curve, where the slope of the curve is determined by $\chi_{PD} (\chi_1 \chi_2)^2$. We re-calibrated the curve fit whenever we changed the size of the matrix-vector product being experimentally computed. See Supplementary Section B for more details on the statistical linear curve fitting methods.

Figure 3(d) shows the experimental matrix-vector multiplication performance of our architecture, where Y is the expected curved-fitted value of the output vector, and \hat{Y} is the experimental output vector. Both Y and \hat{Y} are normalized to the largest value among all the products. First, we characterized scalar-scalar products by computing 10,000 randomized scalar-scalar multiplications and comparing them to the curve fitted analytical product, yielding 9-bit precision. Next, we computed 10,000 randomized 10×10 matrix-vector products to yield 8-bit precision. Thus, we achieved accurate experimental linear matrix-vector products using this architecture.

Nonlinear Characterization

Figure 3(e) illustrates a nonlinear curve fit for a simple intensity-modulated direct detection (IMDD) link, which consists of an electrical input signal $V_X^{(1)}(t)$ being modulated by an MZM and then immediately detected with a photodetector. Our equation that models the output of the IMDD link is:

$$V_{\text{out}}(t) = \chi_0 + \chi_{PD} \chi_1 \sin \left(\chi_2 V_X^{(1)}(t) + \chi_3 \right). \quad (5)$$

Thus, we use a 4-parameter curve fit for the nonlinear characterization (counting $\chi_{PD} \chi_1$ as a single parameter). Figure 3(e) shows an example of curve fitting the analytical model to an experimental characterization of an MZM, where $V_X^{(1)}(t)$ is a 10×1 input vector. For more details and other nonlinear curve fit characterizations, see Supplementary Section C.

3-Layer DNN Inference

We experimentally demonstrated a proof-of-concept of the MAFT-ONN architecture for a 3-layer DNN trained to classify MNIST digits, as shown in Figure 3(a). The outline of the setup is referenced in Figure 3(b), where each photoelectric multiplication implements a fully connected

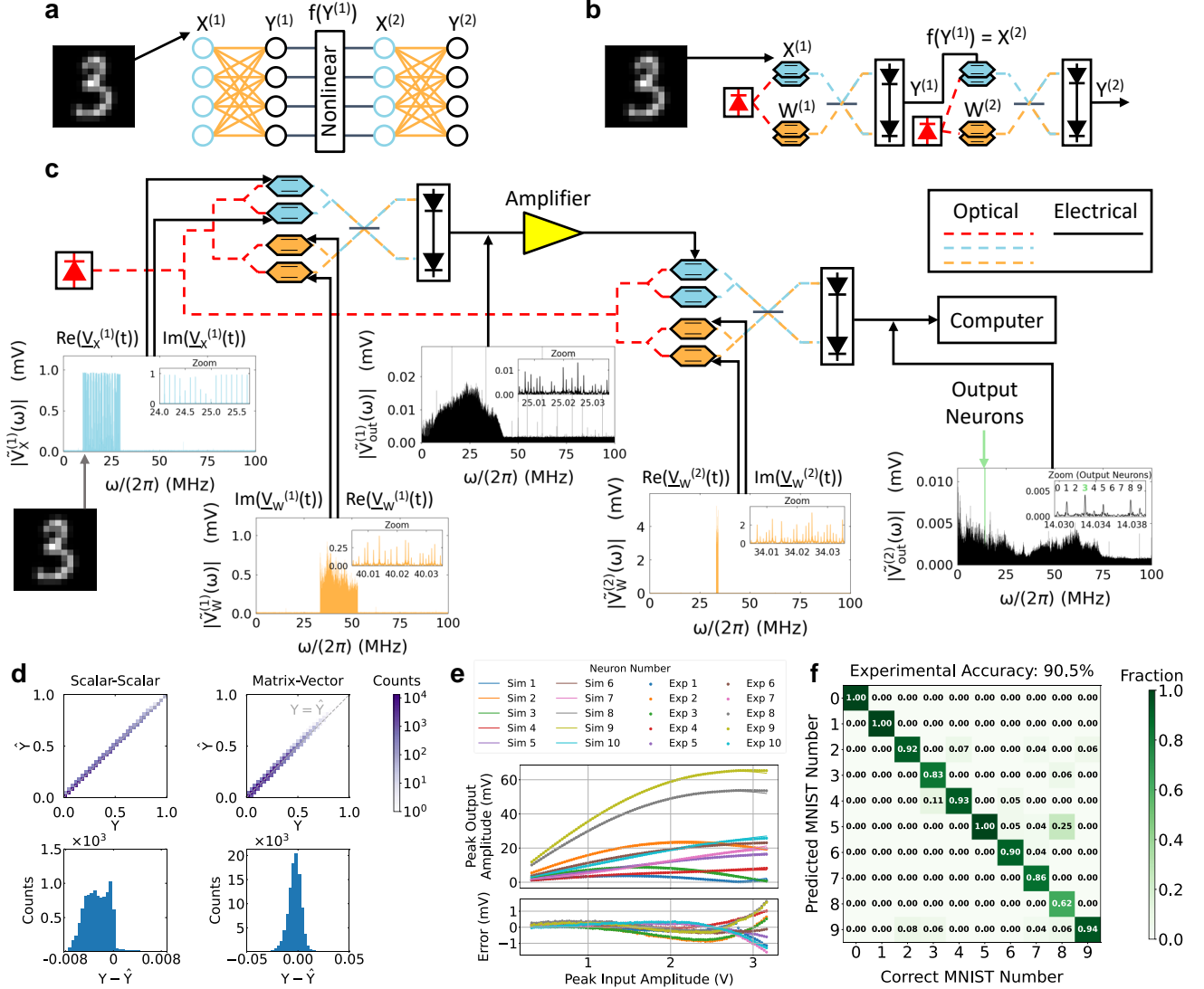


Figure 3. The experimental demonstration of the MAFT-ONN. (a) The structure of a traditional 3-layer DNN. (b) An outline of our 3-layer MAFT-ONN. (c) A more detailed diagram of our 3-layer experiment. The plots show an example of inference, using the 14×14 MNIST image of a "3" shown in (a) as the input vector. The input and weight signals $V_X^{(1)}(t)$, $V_W^{(1)}(t)$, and $V_W^{(2)}(t)$ are generated using an AWG and then modulated onto the laser carrier using DPMZMs in the SSB-SC regime. All plots are the DTFT of the raw time domain data taken from an oscilloscope. The first layer multiplies $V_X^{(1)}(t)$ and $V_W^{(1)}(t)$ with the frequency reduction scheme to yield $V_{out}^{(1)}(t)$. Since we keep the spurious frequencies for training, $V_{out}^{(1)}(t) = V_Y^{(1)}(t)$. The second layer multiplies $V_Y^{(1)}(t)$ (amplified to reach the nonlinear regime of the DPMZM) and $V_W^{(2)}(t)$ with the frequency expansion scheme to yield the final output signal $V_{out}^{(2)}(t)$, which is then read out digitally. As shown in the zoom for plot for $V_{out}^{(2)}(t)$, the image is correctly classified. (d) In the upper half, 2D histograms compare the experimental output values \hat{Y} to the expected curve fitted value Y . In the lower half, 1D histograms plot the error $Y - \hat{Y}$. The scalar-scalar plot contains 10,000 randomized 1×1 matrix products, yielding 9-bit precision compared to the curve fit. The matrix-vector plot contains 10,000 randomized 10×10 matrix products (thus 100,000 values), yielding 8-bit precision. (e) An experimental characterization of the nonlinear activation function of an MZM. We programmed $V_X^{(1)}(t)$ as a 10×1 input vector, and gradually increased its amplitude until it reached the nonlinear regime of the MZM. We then curve fitted an analytical model to the experimental data. (f) A confusion matrix of the experimental 3-layer DNN over 200 14×14 MNIST images, yielding an experimental accuracy of 90.5%.

layer, and the modulator of the second layer implements the nonlinear activation. The first layer uses downsampled 14×14 MNIST images as the input activations, represented by a frequency-encoded signal $V_X^{(1)}(t)$ containing 196 frequencies spaced at 100 kHz. The input activation is fol-

lowed by a hidden layer of 100 neurons represented by a weight signal $V_W^{(1)}(t)$ containing 19,600 frequencies spaced at 1 kHz. The final layer has 10 neurons, one for each of the MNIST digits, and thus the second layer weight signal $V_W^{(2)}(t)$ contains 1,000 frequencies spaced at 1 kHz. As

previously mentioned, we did not filter out the spurious frequencies, and thus trained our DNN on nearly 2 million partial sums.

We implemented the one-hot vector that represents the output MNIST values by randomly selecting a set of 10 adjacent frequencies among the spurious frequencies of $V_{\text{out}}^{(2)}(t)$, to demonstrate the flexibility of our scheme. (See Supplementary Section I for an analysis of choosing random parts of the spectrum for DNN training.) The 10 output neuron frequencies were randomly chosen to be 14.03 MHz to 14.039 MHz, with 1 kHz spacing. The zoom of the plot of $V_{\text{out}}^{(2)}(t)$ in Figure 3(c) shows the mapping of the neuron frequencies to the MNIST digits, where the digit is classified by the frequency mode with that largest magnitude.

Since this scheme performs coherent interferometry, we programmed positive and negative neuron values into both the input vectors and weight matrices. Negative neuron values are physically represented by a π phase shift in that particular frequency mode, allowing for analog matrix algebra with negative numbers.

An analytic model of the hardware was used to train the DNN offline, similar to the nonlinear characterization in the previous section. The offline training produced a set of weight matrices that were then encoded into the RF signals used for the experimental inferences. See Supplementary Sections C and D for details on the offline DNN characterization and training.

The 3-layer experimental DNN inferred 200 14×14 MNIST images, where the digital DNN has an accuracy of 95.5% and the experimental DNN has an accuracy of 90.5%. One contribution to the experimental inaccuracy is the uneven frequency responses of the DPMZMs across the broad bandwidth (see Supplementary Section B), which can be deterministically characterized, improving the accuracy. A higher power low-noise amplified balanced photodetector would also increase the SNR of the signal going into the second layer. Additionally, performing the DNN training in-situ on the hardware itself [35] could help better characterize it and increase the accuracy. The confusion matrix of the experimental DNN is shown in Figure 3(f).

Thus, we have demonstrated for the first time a scalable ONN that implements both the linear and nonlinear operations in-line, where one interferometer implements the single-shot matrix-vector product and one modulator implements the nonlinear activation for an entire layer, enabling scalability in DNN width. In addition, the MAFT-ONN is also scalable in DNN depth due to the ability to directly send the analog output of one layer as the input to the next layer for an arbitrary number of layers, all without digital processing.

DISCUSSION

Time-based Signal Processing

To our knowledge, this MAFT scheme is the first DNN hardware accelerator that is suitable for the direct inference of time-based signals like radio, voice recognition, and biological waveforms, as they are already frequency-encoded

when considering their Fourier transform. In current DNN and ONN architectures, running inference for time-based signals requires the signal to be digitized and pre-processed to be compatible with the hardware, and one must choose how to handle complex-valued data. For example, for RF signal processing, some works process the raw digital IQ data [36], some hand-pick features [37], and some convert the time-based signal into an image using a spectrogram [38]. All of these approaches require digital processing before inference, which is problematic for real-time applications like cognitive radio, voice recognition, and self-driving cars, where ultra-low latency and high-bandwidth throughput are essential.

Computational Throughput

The throughput T measures the number of multiply-and-accumulates (MACs) computed within a given time. The number of MACs performed in a fully connected layer with N input neurons and R output neurons is $N \cdot R$. The time it takes to read out the output vector is the latency, which is $\frac{1}{\min(\Delta f, f_0)}$, where Δf is the smallest frequency spacing of the output signal and f_0 is the lowest neuron frequency of the output signal. (Note that $2\pi f = \omega$, where ω is the angular frequency from the previous sections.) This is also the same as the period of the input, weight, and output signals, and thus the minimum time it takes to create the frequency-encoded signals. Therefore, the throughput is:

$$T = \frac{\# \text{ operations}}{\text{latency}} = N \cdot R \cdot \min(\Delta f, f_0).$$

Let B be the bandwidth available to modulate the input and weight signals. We calculate the throughput in terms of B by plugging in the values of Δf and f_0 based on how the inputs and weight frequencies are programmed. The specific method of programming the inputs and weights is determined by the anti-aliasing conditions that preserve the integrity of the matrix product after the photoelectric multiplication. See Supplementary Section F for the derivation of the anti-aliasing conditions. This analysis yields the throughputs of the frequency reduction and expansion schemes, respectively:

$$T_{\text{reduction}} = \frac{2NR}{3NR + R + 1} B \approx \frac{2}{3} B, \quad (6)$$

$$T_{\text{expansion}} = \frac{R}{1 + R} B \approx B. \quad (7)$$

The approximations for Equations 6 and 7 are valid for $N \gg 1$ and $R \gg 1$, respectively. Therefore, the maximum throughput of this architecture is ultimately limited by the available bandwidth, independent of DNN size. This is because for a given bandwidth limitation B , as the number of neurons increase, the frequency spacing must correspondingly decrease to keep all of the frequencies within the bandwidth. This trade-off yields very similar throughput regardless of the number of neurons or frequency spacing.

In our experiment, we did not filter the signal after layer 1, meaning that we used all the spurious frequencies for

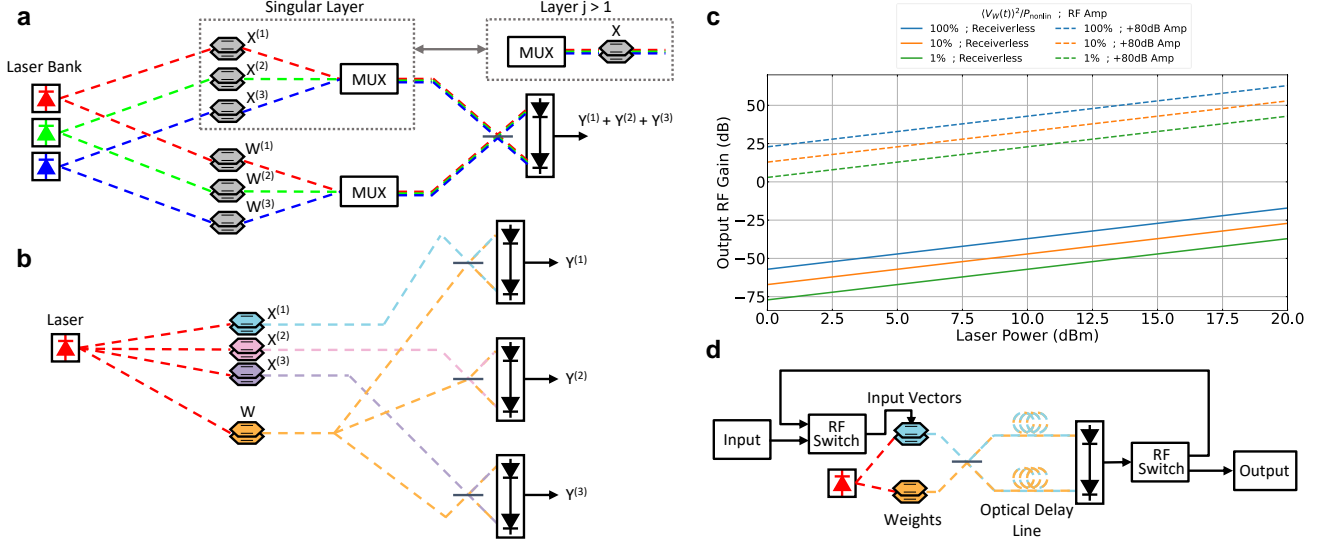


Figure 4. Analysis and future outlook of the MAFT-ONN architecture. (a) A WDM version of this architecture that expands the bandwidth-limited throughput to the wide bandwidth available in optics. Several matrix-vector products can be independently computed on different laser wavelengths, where the WDM output incoherently sums of the independent output vector signals from each laser. (b) A spatially multiplexed version of this architecture that uses optical fan-out to reuse the weight matrix for multiple input vectors. This variant can increase both throughput and energy efficiency. (c) A communication link gain analysis, illustrating the trade-space between the laser power, weight signal power, and RF amplifier gain from Equation 8. The weight signal can be any power as long as it stays within the linear regime of the modulator, where nonlinear power threshold of the modulator is P_{nonlin} . (d) The “loop” version of the MAFT-ONN that can implement an arbitrary number of layers with a signal set of modulators. A fiber delay line can be used to allow time for the RF weight values to update for each layer and for the RF switches to route the data.

DNN training. Note that each spurious frequency contains unique partial sums that are not present in the original matrix-vector product, which is additional information content. Thus, if the throughput calculation were to include these spurious frequencies, then it would be:

$$T_{\text{spurious}} = \frac{\# \text{ operations}}{\text{latency}} = N^2 \cdot R \cdot \min(\Delta f, f_0)$$

$$T_{\text{reduction, spurious}} \approx \frac{2}{3} N \cdot B$$

$$T_{\text{expansion, spurious}} \approx N \cdot B.$$

This spurious throughput is unbounded in N , because in this case, the trade-off from decreasing the frequency spacing to allow for more neurons always results in higher throughput. (Note that the spurious throughput only yields a logarithmic advantage in N when comparing to an operation like the convolution, which uses DTFTs for efficient computation.) Here, the limiting factor is the linewidth of each frequency mode that would prevent adjacent frequencies from being resolved. See Supplementary Section G for the full throughput derivation.

The bandwidth B limiting the throughput is not the RF bandwidth of the electrical components, but the available optical bandwidth. The maximum throughput of this architecture can be realized by: (i) optical wavelength-division multiplexing (WDM) the frequency-encoded signals, or (ii) replacing the frequency-encoded signals with optical frequency combs. For (i), Figure 4(a) illustrates a variant of this architecture that uses optical WDM to simultaneously perform multiple matrix-vector products

each laser on the same photodetector. The incoherence between the lasers allows for each matrix-vector product to independently sum at the photovoltage output. As long as the gap between each laser wavelength is greater than the bandwidth of the photodetector, there will be no cross coupling terms between the matrix-vector products performed on each laser carrier. With the WDM version of the architecture, large matrix products can be tiled in the frequency domain, or matrix-matrix products can be frequency-multiplexed while still computing everything in a single shot. The optical bandwidth can also be used in the case of an arbitrarily deep neural network (the box labeled “Layer $j > 1$ ” in Figure 4(a)), where the same input vector can be independently multiplied by different weight signals for applications like convolution. There is more than 20 THz of available bandwidth among the S, C, and L telecommunication bands (1460nm-1625nm) that can be used here for optical WDM. For (ii), optical frequency combs can replace the WDM modules in Figure 4(a) for even larger throughput. Other works have experimentally demonstrated optical frequency combs with almost 1,000 THz bandwidth [39, 40]. An optical AWG or waveshaper would be required to program the frequency combs.

The throughput can be further increased through spatial multiplexing with copies of the setup running in parallel, shown in Figure 4(b). Other works have demonstrated the viability of densely-packed MZMs, such as a photonic integrated circuit with 48 on-chip MZMs [41]. Therefore, the combination of using the full optical bandwidth (on the order of terahertz) and spatial multiplexing (on the order of a hundred) immediately yields a straightforward path to

reaching peta-operation per second scale throughputs with current technology. Thus, the MAFT-ONN is competitive with electronic counterparts like the Google TPUv3 that has a throughput greater than 400 tera-operations per second [42].

Note that this throughput analysis assumes that the optical bandwidth B is the limiting factor in throughput. See Supplementary Section H for a throughput derivation that is limited to only the electronics without using optical WDM.

Physical Latency

The *physical latency* of this architecture is the time it takes for a signal that is already frequency-encoded to enter the system, go through the optical processing, and then physically leave the system as an electrical output vector signal. (Thus, the time it takes for the signal to travel from the “Analog in” to “Analog out” in Figure 1(a).) This is different from the readout latency described earlier, which is the time it takes to distinguish the frequency modes of the output vector signal. The physical latency of the system in Figure 1(c) with J DNN layers is: $J \cdot (\tau_{MZM} + \tau_{PD} + \tau_{RF} + \tau_{prop})$, where τ_{MZM} is the reciprocal of the bandwidth of the MZM, τ_{PD} is the reciprocal of the bandwidth of the photodetector, τ_{RF} is the combined delay due to the bandwidth of additional RF components like a bandpass filter or amplifier, and τ_{prop} is the data movement in the form of propagation of the frequency-encoded electromagnetic waves.

The value of τ_{MZM} highly depends on the material used for the MZM. State-of-the-art commercial MZMs typically have up to 40 GHz bandwidth, contributing ~ 25 ps delay. The photodetector latency can be separated into the RC time constant and carrier transit time: $\tau_{PD} = \sqrt{\tau_{RC}^2 + \tau_{transit}^2}$ [43]. Whether the RC or carrier transit time will dominate the latency highly depends on the photodetector design. State-of-the-art commercial photodetectors have up to 100 GHz bandwidth, thus contributing ~ 10 ps latency. The value of τ_{RF} is variable and will depend on the use-case; in some scenarios the RF bandpass filter and amplifier are optional. If using a narrow-band RF filter to remove spurious frequencies, then τ_{RF} will strongly dominate the physical latency. Thus, one benefit of keeping the spurious frequencies is to reduce the latency. Finally, the propagation time τ_{prop} is determined by the length of the optical and electrical paths. The frequency-encoded electromagnetic waves will pass through these paths at approximately the speed of light, depending on the refractive index and waveguide properties. The combined length of commercial fiber-optical components typically have tens of centimeters of optical path length after trimming the fiber leads, contributing ~ 300 ps of latency. The electrical RF connections will contribute a similar latency. The optical path length can be shortened to tens of millimeters by implementing this architecture on a photonic integrated circuit [41], reducing the latency to ~ 30 ps. Therefore depending on the scenario, the latency of this architecture will be dominated by data movement at the speed of light,

τ_{prop} .

In our experiment, we measured a latency of 60 ns using DPMZMs with 30 GHz bandwidth, a balanced photodetector with 45 MHz bandwidth, and an RF amplifier with 1 GHz bandwidth. In addition, our experimental setup contains approximately 10 meters of signal propagation, given that standard commercial fiber components have 1 meter fiber leads on each side, plus the length of the RF coaxial cables. Thus, in our experiment, the dominant sources of latency are $\tau_{PD} \approx 1/45$ MHz ≈ 25 ns and $\tau_{prop} \approx \frac{10 \text{ m}}{3 \cdot 10^8 \text{ m/s}} \approx 35$ ns.

The physical latency is independent of the maximum throughput of our system. This is because, as discussed earlier, the throughput is independent of the number of neurons and the frequency spacing. Therefore, for a given physical latency, one can increase the number of neurons (and thus decrease the frequency spacing) until the time it takes to resolve the frequency spacing exceeds the physical latency.

Power Consumption

The power consumption of this architecture primarily depends on the gain of the components and the power of the initial input vector signal. The gain of single layer of this architecture compares the power of an input electrical voltage signal to the power of the output photovoltage signal. It is expressed below [44]:

$$g(\text{linear}) = \frac{\pi^2}{8} \left(\frac{R_{PD} \gamma P_{LD}}{V_\pi} \right)^2 R_i R_o |H_{PD}(f)|^2 \langle V_W^2(t) \rangle \quad (8)$$

where R_{PD} is the responsivity of the photodetector, γ is the gain of the optical link (modulator insertion loss, fiber propagation loss, optical amplifiers, etc.), P_{LD} is the laser power, V_π is the voltage required to reach π phase shift on the modulators, R_i and R_o are the input and output resistances respectively, $H_{PD}(f)$ is the frequency response of the photodetector, and $\langle V_W^2(t) \rangle$ is the time-averaged power of the weight matrix signal. Note that this equation is for a receiverless link (no RF amplifier following the balanced photodetector).

Figure 4(c) illustrates a trade-space between the laser power, the weight signal power, and an RF amplifier. In the plot, V_π is 6 V, R_{PD} is 1 A/W, γ is -6 dB, R_i and R_o are 50 Ω , and H_{PD} is 1/2. Since the power of the weight signal can be adjusted to fit within the linear regime of any modulator, the gain curves are independent of the V_π of the modulators and instead depend on $\langle V_W^2(t) \rangle$. However, the V_π will still determine the threshold of nonlinear regime of the modulator implementing the nonlinear activation.

In our experiment, we found that our DPMZM with $V_\pi \approx 6$ V did not exhibit nonlinear behavior until the input signal reached around $P_{nonlin} = V_\pi^2/R_i \approx 27$ dBm. To alleviate the requirement of high power signals to reach the nonlinear regime, note that in principle, modulators with $V_\pi \approx 1$ mV can be fabricated [45]. In that case, the nonlinear power threshold of the modulator is $P_{nonlin} \approx -47$ dBm. This even allows for input RF signals with -85

dBm of power, which is typically considered the minimum usable power level for communications [46], to be amplified enough to reach the nonlinear regime. Therefore in some scenarios, the gain from the laser may allow for receiverless operation, and in others an amplifier either before or after the modulators may be required.

“Loop” Version

Finally, another variant of this scheme is illustrated in Figure 4(d) that can compute an arbitrary number of DNN layers with a single set of modulators. This “loop” version uses an optical fiber delay lines as temporary optical storage to give time for the RF weights and data routing switches to operate. Just 1 km of commercially available optical fiber used as a delay line is enough to enable MHz-speed RF switches. This version of the architecture can reduce the cost, hardware complexity, and power consumption for computing DNNs with many hidden layers.

CONCLUSION

We introduced and demonstrated a scalable fully-analog deep optical neural net that uses frequency-encoded neurons for the matrix multiplication. The MAFT-ONN scheme yields much flexibility for running various types and sizes of DNNs. The nonlinear activation is performed on a single device, the MZM, making both the linear and nonlinear operations scalable and low-cost. And as demonstrated, this experiment can be quickly assembled with commercial components, greatly increasing the accessibility of ONNs.

This architecture is also the first DNN hardware accelerator that is suitable for the direct inference of temporal data and can achieve real-time inference of the signals with speed-of-light limited latency. When using the full optical bandwidth and spatial multiplexing, the throughput of this system is competitive with other state-of-the-art DNN hardware accelerators.

Outside of DNN hardware acceleration, this architecture also has applications for signal processing. For example, by setting the weight matrix to an identity matrix, this system can take a multi-tone input signal and perform arbitrary frequency transformations without changing the information content of the signal.

Future work includes experimentally implementing the WDM and “loop” variants, and applying this to practical time-based data sets.

ACKNOWLEDGEMENTS

Funding

This work was funded by the Army Research Laboratory Electronic Warfare Branch (Stephen Freeman, Chief), the U.S. Army (W911NF-18-2-0048, W911NF2120099, W911NF-17-1-0527), the U.S. Air Force (FA9550-16-1-0391), MIT Lincoln Laboratory (PO#7000442717), research collaboration agreements with Nippon Telegraph and Telephone (NTT), and the National Science Foundation (NSF) (81350-Z3438201).

Contributions

D.E. and R.D. conceived the idea for the architecture. R.D. conceived the MAFT frequency-encoding and MAFT-ONN hardware setup schemes, developed the theoretical performance metrics, conducted the hardware simulations, and planned and executed the experiment. Z.C. aided with planning and executing the experimental measurements, characterization, debugging, and comparison with the theory. R.D. finalized and analyzed the experimental results. R.H. introduced the idea of using a discrete cosine transform to efficiently model the MZM nonlinearity, and R.D. conceived and created the offline physics-based DNN training algorithm. R.D. wrote the manuscript with contributions from all authors. D.E. supervised the project.

COMPETING INTERESTS

The authors R.D. and D.E. disclose that they are inventors on pending patent US Application No. 63/315,403 where MIT is the patent applicant, which covers the MAFT frequency-encoding scheme and the MAFT-ONN deep neural network hardware architectures described in this work.

DATA AND MATERIALS AVAILABILITY

The data from this work will be made available upon reasonable request.

CODE AVAILABILITY

The code used to curve fit the hardware and train the offline DNN from this work will be made available upon reasonable request.

-
- [1] L. Cai, J. Gao, and D. Zhao, A review of the application of deep learning in medical image classification and segmentation, *Annals of translational medicine* **8** (2020).
 - [2] P. P. Shinde and S. Shah, A review of machine learning and deep learning applications, in *2018 Fourth international conference on computing communication control and*

automation (ICCUBEA) (IEEE, 2018) pp. 1–6.

- [3] Y. Kassahun, B. Yu, A. T. Tibebu, D. Stoyanov, S. Giannarou, J. H. Metzen, and E. Vander Poorten, Surgical robotics beyond enhanced dexterity instrumentation: a survey of machine learning techniques and their role in intelligent and autonomous surgical actions, *International*

- journal of computer assisted radiology and surgery **11**, 553 (2016).
- [4] H. Fujiyoshi, T. Hirakawa, and T. Yamashita, Deep learning-based image recognition for autonomous driving, *IATSS research* **43**, 244 (2019).
 - [5] X. Xu, Y. Ding, S. X. Hu, M. Niemier, J. Cong, Y. Hu, and Y. Shi, Scaling for edge inference of deep neural networks, *Nature Electronics* **1**, 216 (2018).
 - [6] V. Sze, Y.-H. Chen, T.-J. Yang, and J. S. Emer, Efficient processing of deep neural networks: A tutorial and survey, *Proceedings of the IEEE* **105**, 2295 (2017).
 - [7] Y. Shen, N. C. Harris, S. Skirlo, M. Prabhu, T. Baehr-Jones, M. Hochberg, X. Sun, S. Zhao, H. Larochelle, D. Englund, *et al.*, Deep learning with coherent nanophotonic circuits, *Nature Photonics* **11**, 441 (2017).
 - [8] H. Zhu, J. Zou, H. Zhang, Y. Shi, S. Luo, N. Wang, H. Cai, L. Wan, B. Wang, X. Jiang, *et al.*, Space-efficient optical computing with an integrated chip diffractive neural network, *Nature Communications* **13**, 1 (2022).
 - [9] H. Zhang, M. Gu, X. Jiang, J. Thompson, H. Cai, S. Paesani, R. Santagati, A. Laing, Y. Zhang, M. Yung, *et al.*, An optical neural chip for implementing complex-valued neural network, *Nature Communications* **12**, 1 (2021).
 - [10] H. Bagherian, S. Skirlo, Y. Shen, H. Meng, V. Ceperic, and M. Soljacic, On-chip optical convolutional neural networks, arXiv preprint arXiv:1808.03303 (2018).
 - [11] S. Xu, J. Wang, and W. Zou, Optical convolutional neural network with wdm-based optical patching and microring weighting banks, *IEEE Photonics Technology Letters* **33**, 89 (2020).
 - [12] A. N. Tait, T. F. De Lima, E. Zhou, A. X. Wu, M. A. Nahmias, B. J. Shastri, and P. R. Prucnal, Neuromorphic photonic networks using silicon photonic weight banks, *Scientific reports* **7**, 1 (2017).
 - [13] J. Feldmann, N. Youngblood, C. D. Wright, H. Bhaskaran, and W. H. Pernice, All-optical spiking neurosynaptic networks with self-learning capabilities, *Nature* **569**, 208 (2019).
 - [14] V. Bangari, B. A. Marquez, H. Miller, A. N. Tait, M. A. Nahmias, T. F. De Lima, H.-T. Peng, P. R. Prucnal, and B. J. Shastri, Digital electronics and analog photonics for convolutional neural networks (deap-cnns), *IEEE Journal of Selected Topics in Quantum Electronics* **26**, 1 (2019).
 - [15] X. Xu, M. Tan, B. Corcoran, J. Wu, A. Boes, T. G. Nguyen, S. T. Chu, B. E. Little, D. G. Hicks, R. Morandotti, *et al.*, 11 tops photonic convolutional accelerator for optical neural networks, *Nature* **589**, 44 (2021).
 - [16] J. Feldmann, N. Youngblood, M. Karpov, H. Gehring, X. Li, M. Stappers, M. Le Gallo, X. Fu, A. Lukashchuk, A. S. Raja, *et al.*, Parallel convolutional processing using an integrated photonic tensor core, *Nature* **589**, 52 (2021).
 - [17] A. Sludds, S. Bandyopadhyay, Z. Chen, Z. Zhong, J. Cochrane, L. Bernstein, D. Bunandar, P. B. Dixon, S. Hamilton, M. Streshinsky, *et al.*, Delocalized photonic deep learning on the internet's edge, arXiv (2022).
 - [18] R. Hamerly, L. Bernstein, A. Sludds, M. Soljacic, and D. Englund, Large-scale optical neural networks based on photoelectric multiplication, *Physical Review X* **9**, 021032 (2019).
 - [19] T. Wang, S.-Y. Ma, L. G. Wright, T. Onodera, B. C. Richard, and P. L. McMahon, An optical neural network using less than 1 photon per multiplication, *Nature Communications* **13**, 1 (2022).
 - [20] N. H. Farhat, D. Psaltis, A. Prata, and E. Paek, Optical implementation of the hopfield model, *Applied optics* **24**, 1469 (1985).
 - [21] S. Kung and H. Liu, An optical inner-product array processor for associative retrieval, in *Nonlinear Optics and Applications*, Vol. 613 (International Society for Optics and Photonics, 1986) pp. 214–219.
 - [22] J. Ohta, M. Takahashi, Y. Nitta, S. Tai, K. Mitsunaga, and K. Kijima, A new approach to a gaas/algaas optical neurochip with three layered structure, in *Proc. IJCNN International Joint Conference on Neural Networks*, Vol. 2 (1989) pp. 477–482.
 - [23] Y. Zuo, B. Li, Y. Zhao, Y. Jiang, Y.-C. Chen, P. Chen, G.-B. Jo, J. Liu, and S. Du, All-optical neural network with nonlinear activation functions, *Optica* **6**, 1132 (2019).
 - [24] L. Bernstein, A. Sludds, C. Panuski, S. Trajtenberg-Mills, R. Hamerly, and D. Englund, Single-shot optical neural network, arXiv preprint arXiv:2205.09103 (2022).
 - [25] E. Khoram, A. Chen, D. Liu, L. Ying, Q. Wang, M. Yuan, and Z. Yu, Nanophotonic media for artificial neural inference, *Photonics Research* **7**, 823 (2019).
 - [26] F. Ashtiani, A. J. Geers, and F. Aflatouni, An on-chip photonic deep neural network for image classification, *Nature*, 1 (2022).
 - [27] A. N. Tait, T. F. De Lima, M. A. Nahmias, H. B. Miller, H.-T. Peng, B. J. Shastri, and P. R. Prucnal, Silicon photonic modulator neuron, *Physical Review Applied* **11**, 064043 (2019).
 - [28] J. K. George, A. Mehrabian, R. Amin, J. Meng, T. F. De Lima, A. N. Tait, B. J. Shastri, T. El-Ghazawi, P. R. Prucnal, and V. J. Sorger, Neuromorphic photonics with electro-absorption modulators, *Optics express* **27**, 5181 (2019).
 - [29] I. A. Williamson, T. W. Hughes, M. Minkov, B. Bartlett, S. Pai, and S. Fan, Reprogrammable electro-optic nonlinear activation functions for optical neural networks, *IEEE Journal of Selected Topics in Quantum Electronics* **26**, 1 (2019).
 - [30] A. Jha, C. Huang, and P. R. Prucnal, Reconfigurable all-optical nonlinear activation functions for neuromorphic photonics, *Optics Letters* **45**, 4819 (2020).
 - [31] C. Huang, A. Jha, T. F. De Lima, A. N. Tait, B. J. Shastri, and P. R. Prucnal, On-chip programmable nonlinear optical signal processor and its applications, *IEEE Journal of Selected Topics in Quantum Electronics* **27**, 1 (2020).
 - [32] J. Crnjanski, M. Krstić, A. Totović, N. Pleros, and D. Gvozdić, Adaptive sigmoid-like and prelu activation functions for all-optical perceptron, *Optics Letters* **46**, 2003 (2021).
 - [33] J. R. Basani, M. Heuck, D. R. Englund, and S. Krastanov, All-photonic artificial neural network processor via nonlinear optics, arXiv preprint arXiv:2205.08608 (2022).
 - [34] B. Wang, A. Lin, P. Yin, W. Zhu, A. L. Bertozzi, and S. J. Osher, Adversarial defense via the data-dependent activation, total variation minimization, and adversarial training, *Inverse Problems & Imaging* (2020).
 - [35] L. G. Wright, T. Onodera, M. M. Stein, T. Wang, D. T. Schachter, Z. Hu, and P. L. McMahon, Deep physical neural networks trained with backpropagation, *Nature* **601**, 549 (2022).
 - [36] K. Youssef, L. Bouchard, K. Haigh, J. Silovsky, B. Thapa, and C. V. Valk, Machine learning approach to rf transmitter identification, *IEEE Journal of Radio Frequency Identification* **2**, 197 (2018).
 - [37] D. Roy, T. Mukherjee, and M. Chatterjee, Machine learning in adversarial rf environments, *IEEE Communications Magazine* **57**, 82 (2019).
 - [38] J. Ren and X. Jiang, Regularized 2-d complex-log spectral analysis and subspace reliability analysis of micro-doppler

- signature for uav detection, *Pattern Recognition* **69**, 225 (2017).
- [39] D. Lesko, H. Timmers, S. Xing, A. Kowligy, A. J. Lind, and S. A. Diddams, A six-octave optical frequency comb from a scalable few-cycle erbium fibre laser, *Nature Photonics* **15**, 281 (2021).
- [40] F. Couny, F. Benabid, P. Roberts, P. Light, and M. Raymer, Generation and photonic guidance of multi-octave optical-frequency combs, *Science* **318**, 1118 (2007).
- [41] M. Streshinsky, A. Novack, R. Ding, Y. Liu, A. E.-J. Lim, P. G.-Q. Lo, T. Baehr-Jones, and M. Hochberg, Silicon parallel single mode 48×50 gb/s modulator and photodetector array, *Journal of Lightwave Technology* **32**, 3768 (2014).
- [42] S. Kumar, V. Bitorff, D. Chen, C. Chou, B. Hechtman, H. Lee, N. Kumar, P. Mattson, S. Wang, T. Wang, *et al.*, Scale mlperf-0.6 models on google tpu-v3 pods, arXiv preprint arXiv:1909.09756 (2019).
- [43] L. Chrostowski and M. Hochberg, *Silicon Photonics Design: From Devices to Systems* (Cambridge University Press, 2015).
- [44] V. J. Urick, K. J. Williams, and J. D. McKinney, *Fundamentals of microwave photonics* (John Wiley & Sons, 2015).
- [45] M. Hochberg, T. Baehr-Jones, G. Wang, J. Huang, P. Sullivan, L. Dalton, and A. Scherer, Towards a millivolt optical modulator with nano-slot waveguides, *Optics Express* **15**, 8401 (2007).
- [46] D. L. Bhargav, D. Achish, G. Yashwanth, N. P. Kalyan, and K. Ashesh, Prediction of signal drop due to rain at user cellular signal reception, in *Sentimental Analysis and Deep Learning* (Springer, 2022) pp. 357–367.

Supplementary Materials: Frequency-Encoded Deep Learning with Speed-of-Light Dominated Latency

Ronald Davis III¹, Zaijun Chen^{1,3}, Ryan Hamerly^{1,2}, and Dirk Englund¹

¹*Research Laboratory of Electronics, MIT, Cambridge, MA, 02139, USA*

²*NTT Research Inc., PHI Laboratories, 940 Stewart Drive, Sunnyvale, CA 94085, USA and*

³*Ming Hsieh Department of Electrical and Computer Engineering,
University of Southern California, Los Angeles, California 90089, USA*

CONTENTS

| | |
|--|----|
| Experiment | 2 |
| A. 3-Layer DNN Inference | 2 |
| B. Linear Curve Fit Characterizations | 2 |
| AWG Measurements | 3 |
| Scalar-Scalar Product Measurements | 3 |
| Matrix-Vector Product Measurements | 3 |
| C. Nonlinear Curve Fit Characterizations | 4 |
| D. Offline Physics-Based DNN Training | 6 |
| Theory | 7 |
| E. General MAFT Algorithm | 7 |
| F. Anti-Aliasing Conditions | 10 |
| G. Throughput Derivation | 11 |
| H. Non-WDM Throughput Derivation | 13 |
| I. DNN Random Partial Sum Training | 13 |
| J. Time-Multiplexed Matrix-Matrix Products | 14 |

EXPERIMENT

A. 3-Layer DNN Inference

The experimental setup for the 3-layer DNN inference is illustrated in the main text. All of the optics is done in-fiber using commercial components. A total of four DPMZMs are used for the 3-layer experiment. As illustrated in the main text, two pairs of DPMZMs implement the two matrix-vector photoelectric multiplications.

The first set of DPMZMs is from iXblue, where all the fibers both before and after the modulator are polarization-maintaining (PM) with FC/APC leads. The second set of DPMZMs is from Thorlabs, where all the fibers before the modulator are PM, but all the fibers after are single-mode (SM) with FC/PC leads. Thus, we demonstrate that this architecture works with both types of fiber.

Since every DPMZM has 3 DC biases (one for each sub-MZM and then a phase bias for interfering the sub-MZMs together), each of the DPMZMs was controlled using iXblue DPMZM bias controllers, which biased all the DPMZMs for SSB-SC modulation. The bias controller does this by biasing each of the sub-MZMs at their minimum point, and then biasing the phase. Note that the minimum intensity bias point of an MZM is usually highly nonlinear when using a single photodetector. This is because for an electric field $E(t)$, the output of the signal photodetector is proportional to $|E(t)|^2$, the intensity. This means that for a bias ϕ_b , the single photodetector output will yield a bias curve of $\sin(\phi_b)^2 = \frac{1}{2}(1 - \cos(2\phi_b))$. However, the output of a balanced photodetector is proportional to not the intensity, but the electric field $|E(t)|$, yielding a bias curve of $\sin(\phi_b)$. Thus, for a value of $\phi_b = 0$, we see that this is the minimum bias point of the intensity, but is the positive quadrature bias point of the electric field. This conveniently allows us to compute linear matrix operations while operating in the SSB-SC mode.

After setting the bias points for all the modulators, the bias would remain stable for > 24 hours without active control. The Thorlabs DPMZMs require DC-blocks at the RF inputs to stabilize the bias points.

Figure 1 shows how the interferometers are stabilized. The entire experiment is on an optical table that does not have air stabilization. Each interferometer is placed on an optical breadboard that is lifted by vibration-absorbing feet. The surface of each optical breadboard is also covered with vibration-absorbing material on which the fibers and components are placed. The fibers are also taped down to minimize movement. Both interferometers are boxed to reduce temperature and air current fluctuations.

We use one 1550nm external cavity single-frequency laser with a temperature and power controller. The laser is split into four paths; one for each of the DPMZMs. Although the laser is pigtailed with a PM fiber at the output, we observed the best stability when using fiber

polarizers after the laser and before the DPMZMs.

The frequency-encoded RF signals were generated using two Keysight M3202A AWGs. Each DPMZM requires two RF inputs to achieve SSB-SC modulation; one copy of the RF signal at one sub-modulator, and other copy of the RF signal with a 90° phase shift at the other modulator. Thus, two AWG channels were used for each DPMZM. Since one of the DPMZMs is driven by the output of the first layer, we used 6 AWG channels total for the 3-layer inference experiment (not including using one channel to ground the unused sub-MZM on the DPMZM operating in the DSB-SC mode).

For accurate results, the triggers of the AWG signals must be synchronized. This is because any time delay will cause a gradient in the phases between all the frequencies, thus changing the behavior of the photoelectric multiplication. As explained in the main text, we measured a 60ns time delay between the first layer and the second layer, so we programmed the RF signal for the second layer weight matrix with a corresponding time delay. We plan to explore ways to alleviate this synchronization requirement to allow for greater flexibility when using this architecture.

Finally, we used a spectrum analyzer to read the amplitude of the output frequencies for the MNIST inference. We also observed that using an oscilloscope and taking the Fast-Fourier Transform (FFT) of the signal also has accurate readouts, but found using the spectrum analyzer more convenient.

B. Linear Curve Fit Characterizations

All experimental measurements of the neuron frequency modes throughout both the main text and supplementary used a spectrum analyzer (SA), other than the plots in the main text in Figure 2 and Figure 3(c), which used an oscilloscope. Since SAs can only discern the magnitude of each frequency mode and not the phase, all measurements took the absolute value of the actual neuron value. This does not prevent the experiment from computing negative-valued matrix algebra.

All the linear measurements with randomized values that determined a bit precision (Supplementary Figure 2(b) and main text Figure 3(d)) used a single readout from the SA (no averaging). Additionally, the linear curve fits in Figures 3(b) and 3(c) also used a single readout per experimental data point. The frequency correction measurements in 3(d) used the averaging function of the SA to average 100 samples, as that was a one-time deterministic characterization.

All curve fits were computed using the function “curve_fit” from “scipy.optimize” in Scipy version 1.6.2, which provided both the curve fit parameters and the standard deviation errors. Additionally, all curve fits are “double-sided,” allowing for both positive and negative deviations.

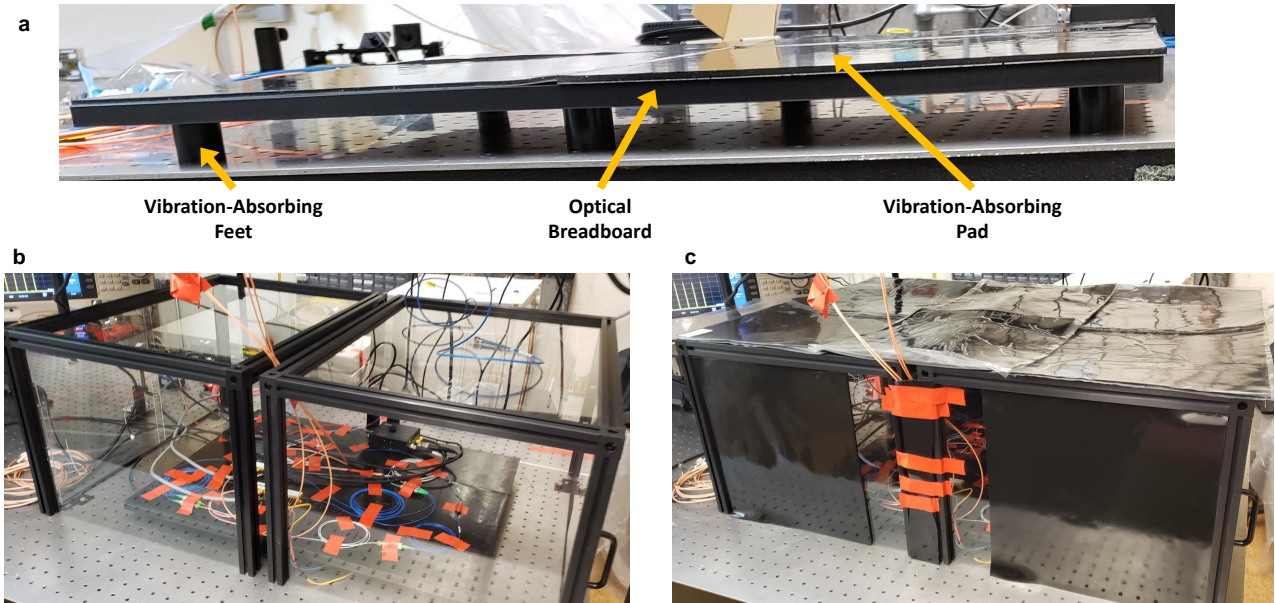


Figure 1. The stabilization of the fiber interferometer that implements the first photoelectric multiplication in the 3-layer DNN experiment. The whole setup is on a single optical table that does not have air stabilization. (a) Each interferometer has its own optical breadboard, supported by vibration-absorbing pads. (b) Each interferometer was boxed to reduce temperature and air current fluctuations. (c) More padding was placed on the box to reduce vibrations.

AWG Measurements

For the linear curve fit, we set a baseline by characterizing the bit-precision of the AWG. Figure 2(a) shows the experimental setup, where the AWG is directly connected to the SA. This experiment consisted of generating single tone 20 MHz sine waves with known amplitudes X , measuring the amplitudes on the SA with a marker set on 20 MHz to yield \hat{X} , then normalizing X and \hat{X} to the largest value, and finally comparing X with \hat{X} . Note that SAs excel at relative frequency measurements, but require calibration for absolute measurements. Thus, we first ran the measurement with 100 randomized values, then deterministically found the calibration factor by adjusting the linear scaling until the bit precision was maximized. The SA calibration factor was found to be ~ 0.68 . We then ran the measurement again with this factor for 1,000 randomized values, where the results are shown in Figure 2(b). We measured a normalized standard deviation of $2.8 \cdot 10^{-4}$ to yield 12-bit precision.

Scalar-Scalar Product Measurements

Figure 3(a) shows the experimental setup used for the scalar-scalar and matrix-vector characterizations in the main text. As described in the main text, we estimated the value of $\chi_{PD} (\chi_1 \chi_2)^2$ using a 1-parameter curve fit for the linear characterizations. We absorb the aforementioned SA calibration factor into all the curve fits.

The scalar-scalar product can be interpreted as a 1×1 matrix-vector multiplication, and thus is set up in the same way as the matrix-vector characterization. We used a single randomized scalar-scalar product to determine the curve fit. The input vector X was randomly set to a 20 MHz sinusoidal wave with peak amplitude of 0.8140314 V. The weight matrix W was randomly set to -0.88271151 V on a 2 MHz sinusoidal wave. Thus the output Y was a 18 MHz sinusoidal wave. Since the AWG has a setting to scale the amplitudes of the signals, we gradually increased the amplitude of X to create the curve in Figure 3(b). The standard deviation error of this curve fit is $8.87 \cdot 10^{-5}$, where the units of the output signal is in volts.

Thus, we accurately computed 10,000 randomized products using a single curve fit from a random scalar-scalar product. This measurement yielded a normalized standard deviation of $2.01 \cdot 10^{-3}$, corresponding to 9-bit precision.

Matrix-Vector Product Measurements

The experimental setup in Figure 3(a) was also used for the matrix-vector product measurements. In this case, the input vector X was a 10-frequency signal from 11 MHz to 20 MHz spaced at 1 MHz. The weight signal W was a 100-frequency signal from 30.6 MHz to 40.5 MHz spaced at 100 kHz.

For this measurement we included a deterministic cor-

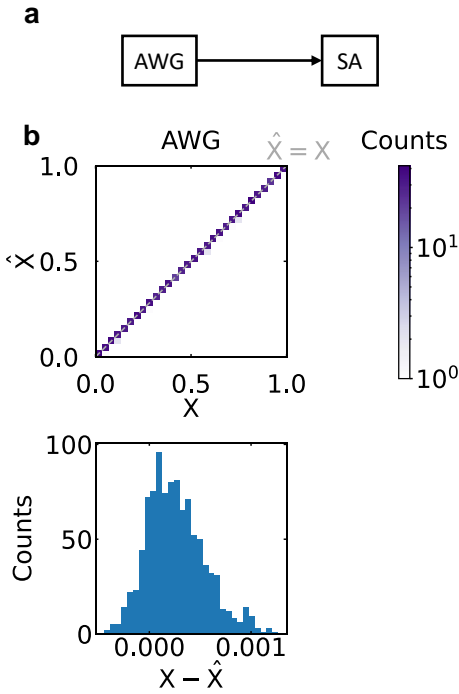


Figure 2. Characterizing the bit-precision of the AWG. (a) The output of the AWG is directly measured by an SA. (b) A comparison between the expected value X and the measured value \hat{X} for 1,000 random scalars, where each scalar is simply the amplitude of a single frequency mode. Above is a 2D histogram comparing the values of X and \hat{X} , and below is a 1D histogram of the error $X - \hat{X}$. This measurement yielded 12-bit precision for the AWG.

rection for the uneven frequency response of the system. After testing different photodetectors and AWGs, we found that it was the DPMZMs that have a significantly varying frequency response even within kHz bandwidth. We individually characterized each DPMZM in the setup illustrated in Figure 3(a) by using the AWG to send a flat RF frequency comb at the frequencies of interest to the DPMZM under test, and then sending a 100 MHz single tone signal to the other DPMZM. This yields an output where the RF frequency comb is simply shifted by 100 MHz, but the shape of the output RF frequency comb reveals the frequency response of the DPMZM under test.

Figure 3(d) shows the result of these measurements. The orange stems are the experimentally measured relative amplitudes of the frequency modes, characterizing the frequency response of the DPMZM. The blue stems are all set to a normalized amplitude of exactly 1 to contrast the orange stems. To apply this correction to the experiment, we multiply X and W by these frequency corrections before generating their signals from the AWG.

With these frequency corrections, we then used a randomized 10×10 matrix-vector product for the curve fit in Figure 3(c). This 1-parameter curve fit yielded a standard deviation error of $2.71 \cdot 10^{-7}$, where the output sig-

nal was in units of volts. At this point there is one last deterministic calibration required, which is to account for the scaling of the AWG. That is, we must scale the peak amplitude of every signal to 1 V before sending it through the AWG (which then has its own amplitude setting). Although this scaling factor is different for every signal, it is deterministic and known beforehand. Thus, we multiply the curve fit parameter found from Figure 3(c) by this scaling factor to find the true parameter of the system.

Then, as explained in the main text, we compute 10,000 randomized 10×10 matrix-vector products, where we apply the AWG scaling to each matrix-vector product. This leads to a normalized standard deviation of $6.43 \cdot 10^{-3}$, corresponding to the 8-bit precision presented in the main text.

C. Nonlinear Curve Fit Characterizations

We characterized the nonlinear behavior of modulators from various manufacturers and configurations to show the accuracy and applicability of our physics-based DNN model. All our nonlinearity characterizations are 4-parameter curve fits to the equation:

$$f(V_X(t)) = \chi_0 + \chi_1 \sin(\chi_2 V_X(t) + \chi_3),$$

where $V_X(t)$ is the input vector signal. Note that we absorb all physical effects into the four parameters above, including χ_{PD} , the SA calibration factor, etc. And like the linear characterizations, all the nonlinear curve fits are also “double-sided.”

Figure 4 shows several configurations for which we curve fitted the nonlinearity. These measurements were performed using the same method as the linear curve fit; by using the AWG amplitude setting to gradually increase the amplitude of the input vector X until it reached the nonlinear regime of the modulator under test. Each configuration within Figure 4 has a different randomized input vector. The DNN algorithm in Supplementary Section D was adjusted to match each curve fit configuration. All configurations except the one in Figure 4(e) used the frequency correction method described in Supplementary Section B. An RF amplifier was used for all configurations to increase the power of the electrical signal to reach the nonlinear regime of the modulator under test. Table I shows the standard deviation error of the various nonlinear curve fits. All measurements in Figures 4(a)-(d) used the averaging function of the SA to average 50 samples for each experimental data point. The data points in the 3-layer DNN characterization measurement in Figure 4(e) did not use the SA averaging feature, instead using a single SA readout per experimental data point.

Figure 4(a) is a simple IMDD link, using a regular MZM biased at quadrature (not a DPMZM). All other configurations exclusively use DPMZMs. This MZM has

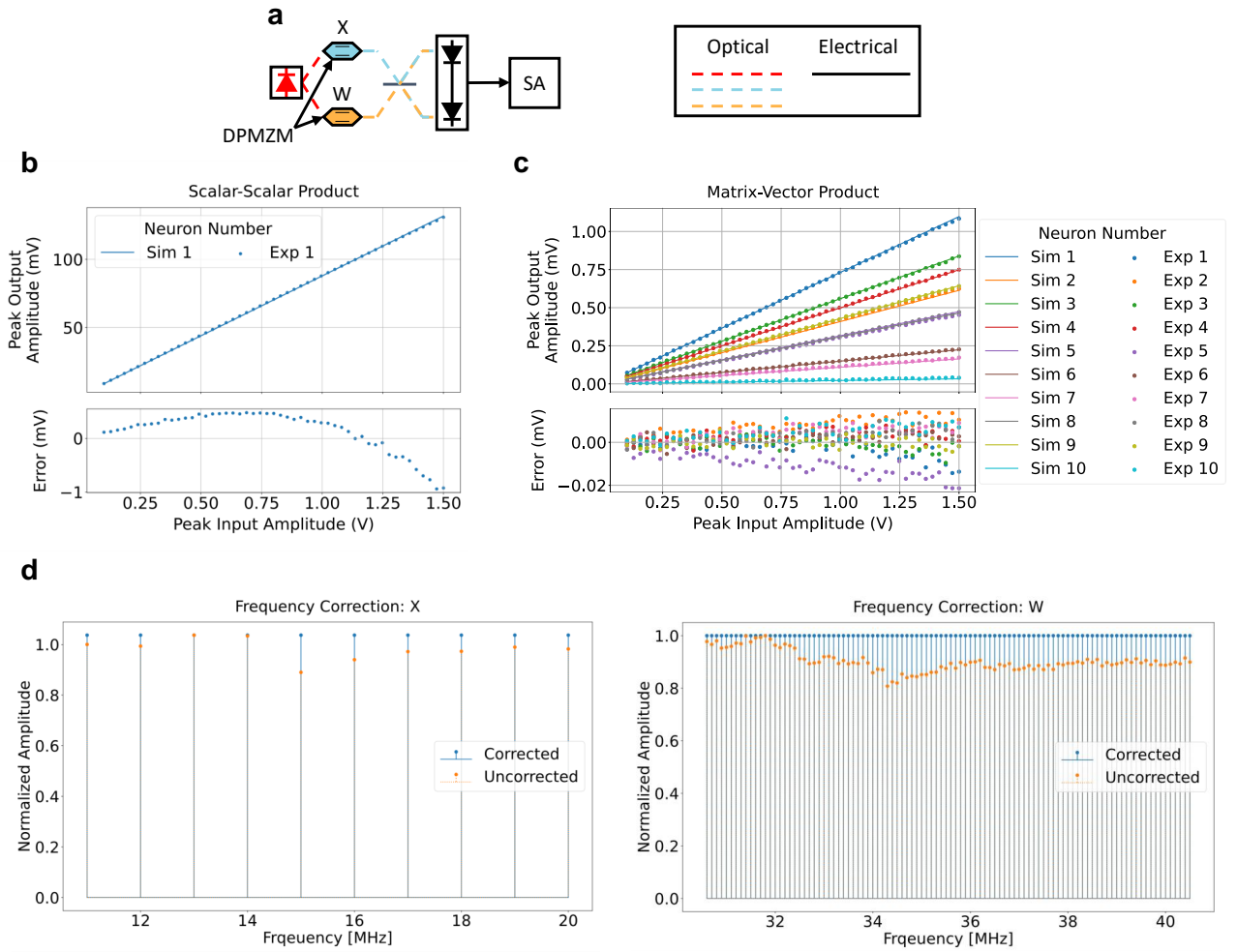


Figure 3. The linear matrix-vector characterizations. (a) The experimental setup for the linear characterization. (b) The curve fit used for the scalar-scalar characterization in the main text. (c) The curve fit used for the matrix-vector characterization in the main text. (d) The deterministic corrections to account for the uneven frequency response of the DPMZMs for the matrix-vector characterization in (c).

| Figure | χ_0 Error | χ_1 Error | χ_2 Error | χ_3 Error |
|--------|----------------------|----------------------|----------------------|----------------------|
| 4(a) | $4.52 \cdot 10^{-4}$ | $1.05 \cdot 10^{-5}$ | $7.71 \cdot 10^{-4}$ | $1.91 \cdot 10^{-2}$ |
| 4(b) | $1.36 \cdot 10^{-3}$ | $4.67 \cdot 10^{-4}$ | $1.33 \cdot 10^{-3}$ | $3.37 \cdot 10^{-2}$ |
| 4(c) | $7.01 \cdot 10^{-5}$ | $1.41 \cdot 10^{-5}$ | $6.24 \cdot 10^{-4}$ | $8.65 \cdot 10^{-3}$ |
| 4(d) | $5.73 \cdot 10^{-5}$ | $1.66 \cdot 10^{-5}$ | $1.17 \cdot 10^{-3}$ | $9.34 \cdot 10^{-3}$ |
| 4(e) | $1.11 \cdot 10^{-2}$ | $4.00 \cdot 10^{-4}$ | $6.17 \cdot 10^{-2}$ | $2.08 \cdot 10^{-2}$ |
| 5(a) | $2.89 \cdot 10^{-4}$ | $2.48 \cdot 10^{-5}$ | $7.31 \cdot 10^{-4}$ | $1.43 \cdot 10^{-2}$ |
| 5(b) | $1.66 \cdot 10^{-4}$ | $6.25 \cdot 10^{-5}$ | $1.02 \cdot 10^{-4}$ | $2.05 \cdot 10^{-2}$ |
| 6 | $8.89 \cdot 10^{-5}$ | $1.69 \cdot 10^{-5}$ | $1.77 \cdot 10^{-3}$ | $1.13 \cdot 10^{-2}$ |

Table I. The one standard deviation errors of the nonlinear curve fits for the various configurations, where the units of the output signal is volts.

a polarization-maintaining (PM) fiber lead input and a single-mode (SM) fiber lead output. Thus, all optical fibers before the MZM are PM, and the ones after are SM. The input vector signal $V_X(t)$ contained 10 frequencies from 100 MHz to 109 MHz spaced at 1 MHz. A single (non-balanced) photodetector was used here.

Figure 4(b) has the same configuration as that in Figure 4(a), except the MZM is replaced with a DPMZM with a PM output fiber lead. For all configurations with DPMZMs, we characterize the nonlinearity by driving only one of the sub-MZMs. In this case, we used the bias controller to set the DPMZM to the SSB-SC mode that sets both sub-MZMs to their minimum bias point. Then we manually changed the bias point of the sub-MZM under test to quadrature. The frequencies of $V_X(t)$ are the same as in 4(a), but with a different set of randomized

values. This is the nonlinear characterization shown in the main text.

Figure 4(c) uses an interferometer configuration with two DPMZMs, testing the nonlinear behavior with photoelectric multiplication. Here, the DPMZMs have an SM fiber output lead, and thus all fibers after the DPMZMs are SM. As explained in Supplementary Section A, all sub-MZMs were biased at their minimum point. Here, $V_X(t)$ is a 10-frequency signal from 10 MHz to 19 MHz spaced at 1 MHz with randomized values. And similar to the linear characterization, we set $V_W(t)$ to be a single tone at 50 MHz, measuring the output signal from 60 MHz to 69 MHz.

Figure 4(d) has the same hardware configuration and parameters as (c), except that we used DPMZMs with PM fiber output leads, and thus used PM fibers throughout the whole configuration. We consistently observed a ripple with this configuration, which is discussed later with Figure 6. This is same the configuration used for the linear characterization in Supplementary Section B (excluding the RF amplifier).

Figure 4(e) is the same configuration as the 3-layer experiment in the main text. This figure shows the curve fit that was used to infer the 200 MNIST images. The SA measurements for both the curve fit and the MNIST inference experiment in the main text were single readouts without averaging. For this curve fit, the values of $X^{(1)}$, $W^{(1)}$, and $W^{(2)}$ were all randomized. For the MNIST inference and DNN training, the nonlinearity was programmed at the strongest setting (the right-most set of data points).

Figure 5 repeats the measurement for two of the configurations from Figure 4, except setting $V_X(t)$ to be a 49-frequency signal (the same size as a downsampled 7×7 MNIST image) from 10.1 MHz to 14.9 MHz with 100 kHz spacing, with randomized values. The configuration in Figure 5(b) again sets $V_W(t)$ to be a single tone at 50 MHz. We plot the nonlinear curves of all 49 neurons, thus demonstrating a larger scale nonlinearity.

Figure 6 explores the ripples observed in the nonlinear characterization of the hardware configuration in Figure 4(d). Here, the curve fit was only applied to the top left measurement, and the same parameters were used for the other three measurements. All four measurements were taken within 40 minutes. Here, we see that the number and position of the ripples vary per measurement. We hypothesize that the ripples are caused either by (i) interference due to imperfect attenuation of the laser carrier and sideband that allows for SSB-SC modulation or (ii) optical path length imbalance in the interferometer. If the cause is (i), then this can perhaps be rectified by achieving SSB-SC modulation using a passive optical filter or a different bias control scheme. For (ii), then introducing efforts to balance the optical paths may help.

D. Offline Physics-Based DNN Training

For the 3-layer DNN experiment, the DNN was trained offline using an analytic model of the hardware. As explained in the main text, four parameters were curve fitted to the experimental hardware. One challenge was to create a DNN training algorithm that accurately models the photoelectric multiplication and nonlinearity while being fast enough to train the DNN in a reasonable time.

Pytorch was used for the DNN training, as the software automatically calculates the gradients for training the parameters, as long as only Pytorch functions are used to model the physics. Algorithm 1 shows the pseudocode to quickly model the physics of the system. We briefly explain each of the steps:

Algorithm 1: Physics-Based DNN Training

```

1:  $\Delta f \leftarrow \text{GCD}(\text{List of Expected Frequencies})$ 
2:  $\bar{X}^{(1)}(f), \bar{W}^{(1)}(f), \bar{W}^{(2)}(f) \leftarrow \text{DNN Matrix Values}$ 
3:  $X^{(1)}(t), X_{\text{shift}}^{(1)}(t) \leftarrow \text{DCT}(\bar{X}^{(1)}(f)), \text{DCT}_{\text{variant}}(\bar{X}^{(1)}(f))$ 
4:  $W^{(1)}(t), W_{\text{shift}}^{(1)}(t) \leftarrow \text{DCT}(\bar{W}^{(1)}(f)), \text{DCT}_{\text{variant}}(\bar{W}^{(1)}(f))$ 
5:  $W_{\text{shift}}^{(2)}(t) \leftarrow \text{DCT}_{\text{variant}}(\bar{W}^{(2)}(f))$ 
6:  $Y^{(1)}(t) \leftarrow X^{(1)}(t)W_{\text{shift}}^{(1)}(t) - X_{\text{shift}}^{(1)}(t)W^{(1)}(t)$ 
7:  $f(Y^{(1)}(t)) \leftarrow \chi_0 + \chi_1 \sin(\chi_2 Y^{(1)}(t) + \chi_3)$ 
8:  $X^{(2)}(t) \leftarrow f(Y^{(1)}(t))$ 
9:  $Y^{(2)}(t) \leftarrow X^{(2)}(t)W_{\text{shift}}^{(2)}(t)$ 
10:  $\bar{Y}^{(2)}(f) \leftarrow \text{DCT}(Y^{(2)}(t))$ 

```

1. Taking the greatest common denominator (GCD) of some frequencies we expect to be present to discretize the frequency space
2. Directly inserting the vector and matrix values into the frequency domain
3. Converting the inputs to the time domain, where the "shift" of the signal is the 90° shifted signal used for SSB-SC modulation, and the "variant" of the discrete cosine transform (DCT) is an altered version of the DCT that yields the desired 90° shifted signal
4. Converting the layer 1 weights to the time domain
5. Converting the layer 2 weights to the time domain
6. The linear output of the first photoelectric multiplication; this signal contains the spurious frequencies, which can be filtered out at this point if desired
7. Applying the curve fitted nonlinear activation
8. The nonlinear output of the first layer is the input to the second layer
9. The second photoelectric multiplication, modeling the photoelectric multiplication of the input in the DSB-SC mode and the weights in the SSB-SC mode

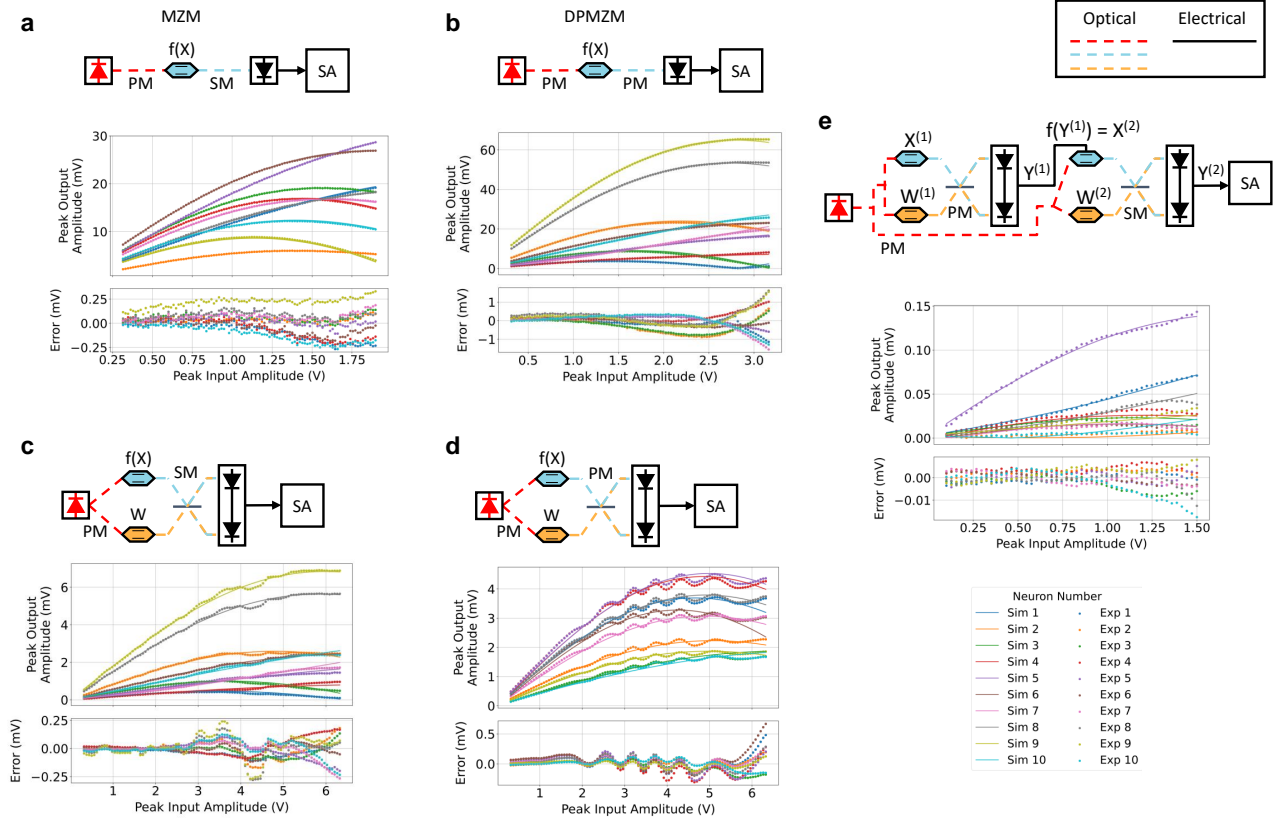


Figure 4. Various configurations for characterizing the MZM nonlinearity.

10. Converting the output to the frequency domain to retrieve the neuron values

We also included the effects of the AWG scaling and the frequency correction mentioned in Supplementary Section B into the algorithm, depending on the hardware configuration being modeled. And although we did not use any frequency filters for our experiments, we incorporated the effects of attenuation from a filter into the DNN model.

The physics-based DNN training was found to take up to approximately 5-6 times longer to train compared to a conventional DNN, depending on the workload. A better optimized physics-based algorithm should be able to cut the time down.

THEORY

E. General MAFT Algorithm

The input and output frequencies do not have to be evenly spaced like they are in the main text. We used the even frequency spacing in the main text to maximize the throughput, which is limited by the time required

to resolve the smallest frequency spacing. This general frequency-encoding algorithm will show that a set of input frequencies can be transformed to an arbitrary set of output frequencies while computing an arbitrary matrix-vector product $WX = Y$, where W has size $(R \times N)$, X has size $(N \times 1)$, and Y has size $(R \times 1)$. This can all be accomplished in a single shot in the frequency domain.

As in the main text, we will assume that the input activation signal has frequency spacing $\Delta\omega_X$ and offset $n_0 \cdot \Delta\omega_X$; hence, the input vector begins as the electrical voltage signal $V_X(t) = \sum_{n=1}^N X_n \cos((n_0 + n)\Delta\omega_X t)$. Here we assume equal frequency spacing for the input signal for convenience, without loss of generality. The input signal can express an arbitrary set of frequencies by decreasing $\Delta\omega_X$ and setting the non-occupied frequencies to zero. Now we do not assume anything about the output signal frequencies, leaving the weight frequencies as arbitrary values. Therefore, let the frequency corresponding to the weight matrix element $W_{r,n}$ be $\omega_{r,n}^W$. This yields the electrical voltage signal for the weight matrix: $V_W(t) = \sum_{r=1}^R \sum_{n=1}^N W_{r,n} \cos(\omega_{r,n}^W t)$.

Next, $V_X(t)$ and $V_W(t)$ are SSB-SC modulated onto a laser carrier with frequency ω_{LD} . This yields (ignoring linear scaling factors):

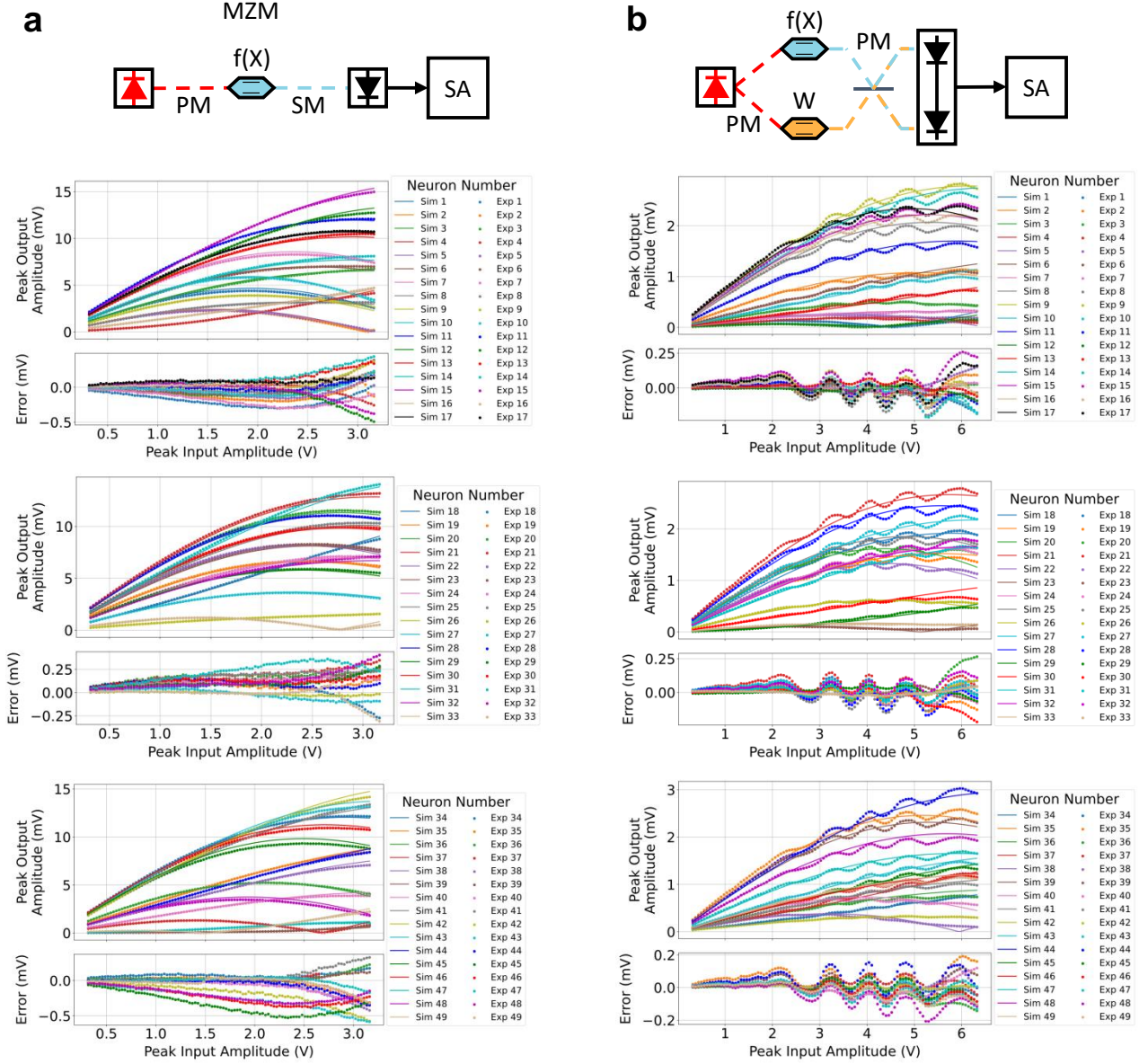


Figure 5. A 49-frequency (size of an downsampled 7×7 MNIST image) nonlinear characterization, where we plot the nonlinear curves of all 49 neurons for two configurations from Figure 4.

$$E_X(t) \propto \sum_{n=1}^N X_n e^{i((n_0+n)\Delta\omega_X + \omega_{LD})t},$$

$$E_W(t) \propto \sum_{r=1}^R \sum_{n=1}^N W_{r,n} e^{i(\omega_{r,n}^W + \omega_{LD})t}.$$

Next, the optical fields $E_X(t)$ and $E_W(t)$ enter a 2×2 50:50 beam splitter and then a balanced photodetector for the photoelectric multiplication. The optical outputs

of the beam splitter are:

$$E_{BS1}(t) \propto E_X(t) - iE_W(t),$$

$$E_{BS2}(t) \propto -iE_X(t) + E_W(t).$$

Then $E_{BS1}(t)$ and $E_{BS2}(t)$ each enter a photodetector, and the outputs are subtracted to yield the photoelectric multiplication output (again ignoring scaling factors):

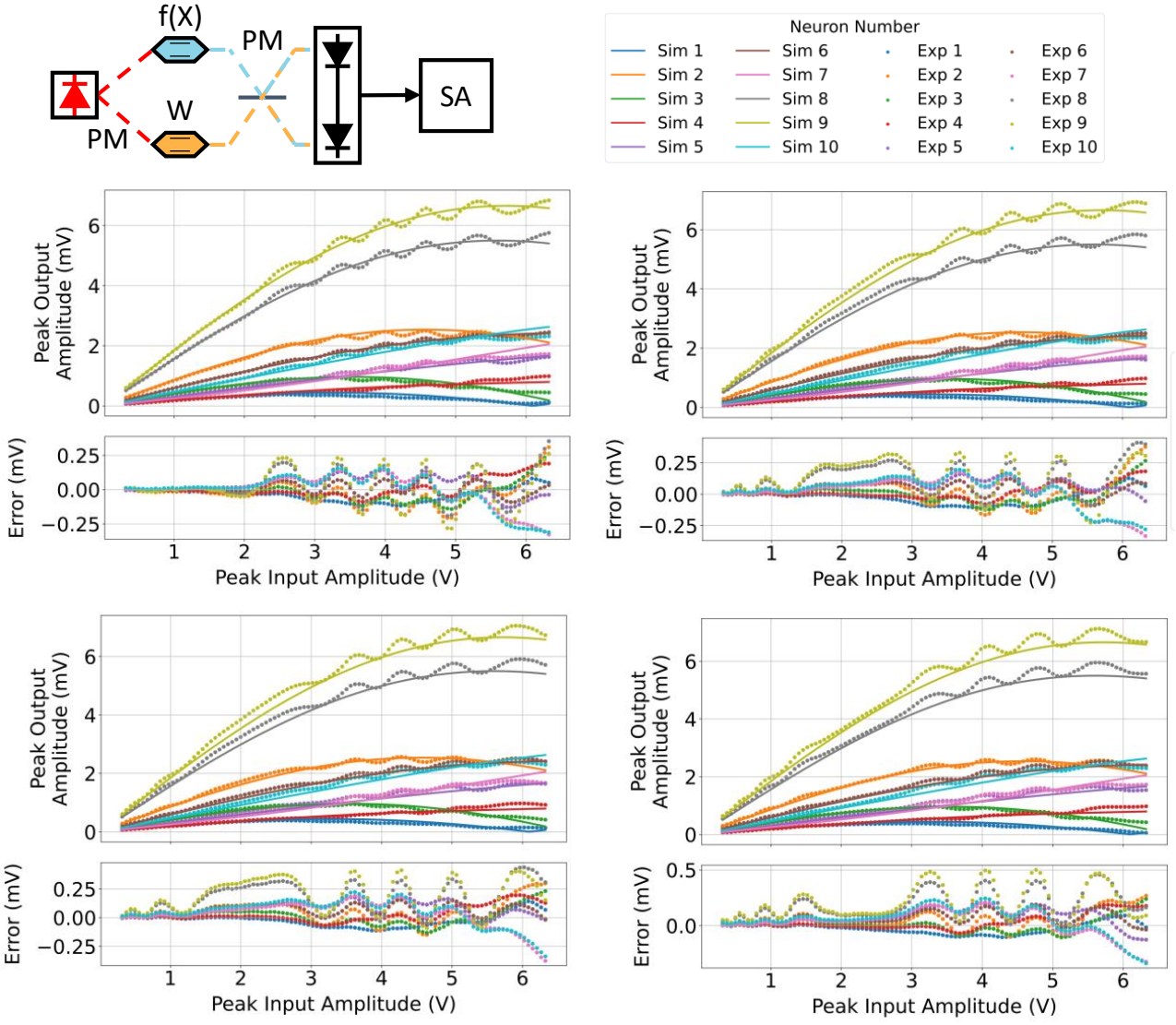


Figure 6. A nonlinear measurement that was repeated four times to explore the nature of the ripples observed in Figure 4(d). The curve fit parameters are the same for all four experiments and were derived from the top left measurement.

$$\begin{aligned}
 V_{\text{out}}(t) &\propto |E_{\text{BS1}}(t)|^2 - |E_{\text{BS2}}(t)|^2 \\
 &\propto \text{Im} [E_X^*(t)E_W(t)] \\
 &\propto \text{Im} \left[\sum_{r=1}^R \sum_{n'=1}^N \sum_{n=1}^N W_{r,n'} X_n e^{i((\omega_{r,n'}^W - (n_0+n)\Delta\omega_X)t)} \right] \\
 &\propto \sum_{r=1}^R \sum_{n'=1}^N \sum_{n=1}^N W_{r,n'} X_n \sin((\omega_{r,n'}^W - (n_0+n)\Delta\omega_X)t)
 \end{aligned} \tag{1}$$

Everything so far in this analysis has only considered the physics of the system. Now we can choose the interpretation of the signals to represent matrix-vector prod-

uct. By definition of matrix multiplication, the output matrix elements are: $Y_r = \sum_{n=1}^N W_{r,n} X_n$. By comparing this definition of a matrix product to Equation 1, we see that only the frequencies that correspond to $n' = n$ will contribute to the desired operation. All other frequencies will be spurious. There are a total of RN^2 unique partial sums generated by this photoelectric multiplication.

This matrix-vector product can be achieved by programming the weight frequencies to group some of the RN^2 partial sums into R groups of N frequencies. Each group is associated with a value r and thus the element of the output matrix Y_r . Say that we want to map each output matrix element Y_r to frequency ω_r^Y . Then the solution for the weight matrix frequencies to achieve this

desired frequency transformation is:

$$\omega_{r,n'}^W = \omega_r^Y + (n_0 + n')\Delta\omega_X, \quad (2)$$

for $n' \in [1, \dots, N], r \in [1, \dots, R]$. Plugging Equation 2 into Equation 1, we have:

$$V_{\text{out}}(t) \propto \sum_{r=1}^R \sum_{n'=1}^N \sum_{n=1}^N W_{r,n'} X_n \sin((\omega_r^Y + (n' - n)\Delta\omega_X)t) \quad (3)$$

$$\begin{aligned} &\propto \sum_{r=1}^R \sum_{n=1}^N W_{r,n} X_n \sin(\omega_r^Y t) \\ &\quad + \sum_{r=1}^R \sum_{n'=1}^N \sum_{\substack{n=1 \\ n \neq n'}}^N W_{r,n'} X_n \sin((\omega_r^Y + (n' - n)\Delta\omega_X)t) \end{aligned}$$

$$\propto \sum_{r=1}^R Y_r \sin(\omega_r^Y t) \quad (4)$$

$$\begin{aligned} &\quad + \sum_{r=1}^R \sum_{n'=1}^N \sum_{\substack{n=1 \\ n \neq n'}}^N W_{r,n'} X_n \sin((\omega_r^Y + (n' - n)\Delta\omega_X)t) \\ &\propto V_Y(t) + V_S(t), \end{aligned} \quad (5)$$

where we ignore the linear scaling factor, which is discussed in the main text. From Equation 4 to Equation 5, we group the terms with $n' = n$ as the output vector Y , described as $V_Y(t)$ and the terms with $n' \neq n$ as the ‘spurious frequency’ components $V_S(t)$.

Thus, by programming the weight signal accordingly, we perform both a matrix-vector product and frequency transformation. The electric voltage output signal is $V_Y(t) = \sum_{r=1}^R Y_r \sin(\omega_r^Y t)$, and the remainder of the signal contains the spurious frequencies. We arrive to the same equations in the main text by choosing equally spaced output vector frequencies: $\omega_r^Y = (r_0 + r)\Delta\omega_Y$.

F. Anti-Aliasing Conditions

The frequency reduction and expansion schemes from the main text use the result from Equation 4 in a way that prevents aliasing—when some of the spurious frequencies overlap with the output vector frequencies. Each scheme avoids aliasing in a different way. Recall that in both schemes, $\omega_r^Y = (r_0 + r)\Delta\omega_Y$, as in the main text.

First, we analyze the anti-aliasing conditions of the frequency reduction scheme. Here, the frequency spacing of the output frequencies are less than that of the input frequencies: $\Delta\omega_Y < \Delta\omega_X$. As Figure 7 illustrates, there are two types of aliasing that must be avoided.

The first type of aliasing, shown in Figure 7(a), originates from the overlapping of the spurious frequencies

with the output vector frequencies. We find the anti-aliasing constraint by keeping track of the distance of the closest spurious frequency to the edge of band of output vector frequencies. From Equation 4, the lowest spurious frequency after the band is $(r_0 + 1)\Delta\omega_Y + \Delta\omega_X$, and the highest output vector frequency is $(r_0 + R)\Delta\omega_Y$. Thus, as labeled in Figure 7(a) the gap between these frequencies is $\Delta\omega_X + (1 - R)\Delta\omega_Y$. Hence, for anti-aliasing, this gap must be greater than 0 at minimum. This yields the constraint: $\Delta\omega_Y < \frac{1}{R-1}\Delta\omega_X$. A reasonable design choice, which is the one we made for the experiment, is to set this gap equal to the smallest frequency spacing already present in the signal, $\Delta\omega_Y$. So with this anti-aliasing condition we get: $\Delta\omega_Y = \frac{1}{R}\Delta\omega_X$.

The second anti-aliasing condition comes from the fact that the signal is real, and thus, in the frequency domain, it is possible for the negative part of the signal to creep into the positive region. This phenomenon is conveyed in Figure 7(b). Here, we calculate the gap between the lowest output vector frequency and the least-negative spurious frequency. The former is $(r_0 + 1)\Delta\omega_Y$. The latter, according to Equation 4, is $-((1 - N)\Delta\omega_X + (r_0 + 1)\Delta\omega_Y)$. Therefore, as labeled in Figure 7(b) the frequency gap is $2(r_0 + 1)\Delta\omega_Y - (N - 1)\Delta\omega_X$. Again, we want this gap to be greater than 0 to avoid aliasing, so we end up with the constraint $(r_0 + 1)\Delta\omega_Y > \frac{1}{2}(N - 1)\Delta\omega_X$. Another reasonable design choice is to also set this gap equal to $\Delta\omega_Y$. Applying both design choices, we solve for the term r_0 to get: $r_0\Delta\omega_Y = \frac{1}{2}(N - \frac{R+1}{R})\Delta\omega_X$. Now we have a set of constraints and a way to program the weight signal frequencies to guarantee that the spurious frequencies do not overlap with the output vector frequencies when using the frequency reduction scheme.

Next is the frequency expansion scheme, where the output vector frequency spacing is larger than the input frequency spacing; $\Delta\omega_Y > \Delta\omega_X$. Figure 8 illustrates the anti-aliasing conditions. The two types of aliasing here are the same as in the frequency reduction scheme.

For the first type of aliasing, showed in Figure 8(a), we calculate the frequency gap between the j^{th} output vector frequency and the closest spurious frequency. The frequency of the j^{th} output vector is $(r_0 + j)\Delta\omega_Y$, and the closest spurious frequency is $(r_0 + j - 1)\Delta\omega_Y + (N - 1)\Delta\omega_X$. (The spurious frequencies are symmetric about each output vector frequency, so this calculation can also be done with the higher spurious frequency.) Thus, the frequency gap is $\Delta\omega_Y - \Delta\omega_X(N - 1)$. Therefore, the anti-aliasing condition is: $\Delta\omega_Y > \Delta\omega_X(N - 1)$. And another reasonable design choice is to set this gap equal to the smallest frequency spacing present in the signal, $\Delta\omega_X$. With this, we get: $\Delta\omega_Y = N\Delta\omega_X$.

Figure 8(b) shows the second type of aliasing for the frequency expansion scheme, where the negative frequencies of the real signal creep into the position region. The constraint arising from this aliasing is derived in the same way. The lowest output vector frequency is $(r_0 + 1)\Delta\omega_Y$, and the least-negative spurious frequency

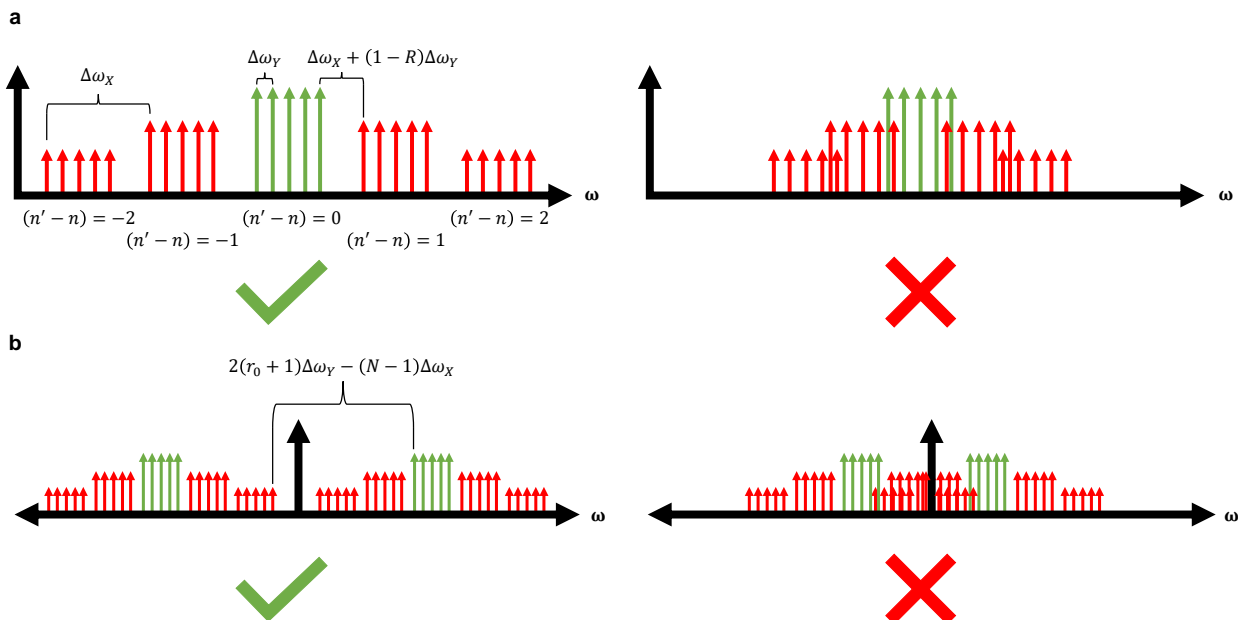


Figure 7. The anti-aliasing conditions for the frequency reduction scheme, where the output vector frequencies are green and the spurious frequencies are red. (a) The first type of aliasing comes from the spurious frequencies overlapping with the output vector frequencies. This can be avoided by decreasing the output frequency spacing. (b) The second type of aliasing comes from the negative frequencies creeping up to the positive region. This can be avoided by increasing output frequency offset.

is $-((1 - N)\Delta\omega_X + (r_0 + 1)\Delta\omega_Y)$. Thus, the frequency gap is $2(r_0 + 1)\Delta\omega_Y - (N - 1)\Delta\omega_X$, yielding the anti-aliasing constraint: $(r_0 + 1)\Delta\omega_Y > \frac{1}{2}(N - 1)\Delta\omega_X$. Interestingly, when using the design choice from above, this constraint becomes $r_0\Delta\omega_Y > -\frac{1}{2}(N - 1)\Delta\omega_X$. Since the constraint is a negative number, we can simply set the offset frequency for the output vectors to zero as a convenient design choice, so $r_0 = 0$.

As shown above, the spurious frequencies generated by the photoelectric multiplication requires anti-aliasing conditions to ensure they do not degrade the matrix-vector product. In addition to the constraints, we also presented some convenient design decisions for handling the spectrum. These design decisions do not have to be followed, however. For example, for our experiment, in the layer 1 frequency reduction scheme, we chose a value of r_0 that was larger than necessary in order to push all the frequencies beyond 2 MHz, which is the lower limit of our RF amplifier.

G. Throughput Derivation

The throughput is a measure of the volume of data that can be processed within a given time. Since this architecture directly computes matrix-vector products, we analyze the throughput of a single fully-connected layer of a DNN. From the main text, the general throughput

equation is:

$$T = \frac{\# \text{ operations}}{\text{latency}} = N \cdot R \cdot \min(\Delta f, f_0), \quad (6)$$

where N is the number of input neurons into the layer, R is the number of output neurons, Δf is the smallest spacing of the output signal, and f_0 is the lowest neuron frequency of the output signal. Here we derive the throughput for the frequency reduction and expansion schemes, given the anti-aliasing conditions found in the previous section.

The available bandwidth with which to modulate the inputs and weights, B , limits the weight matrix signal, as that signal will always have a higher frequency than the input signal, as shown in Equation 2. Therefore, the maximum bandwidth used to modulate the signals is: $B = (n_0 + N)\Delta f_X + (r_0 + R)\Delta f_Y$. As we saw in Supplementary Section E, the term n_0 cancels out and does not affect the output frequencies. So as a design choice to maximize the available bandwidth, we set $n_0 = 0$ to yield $B = N\Delta f_X + (r_0 + R)\Delta f_Y$.

For the frequency reduction scheme, it is clear that the limiting factor in the term $\min(\Delta f, f_0)$ is the frequency spacing of the output signal, Δf_Y . This is because by definition the frequency reduction scheme requires that $\Delta f_Y < \Delta f_X$, and we see from the anti-aliasing conditions that $\Delta f_Y < r_0\Delta f_Y$. Hence, the throughput of the frequency reduction scheme is: $T_{\text{reduction}} = N \cdot R \cdot \Delta f_Y$.

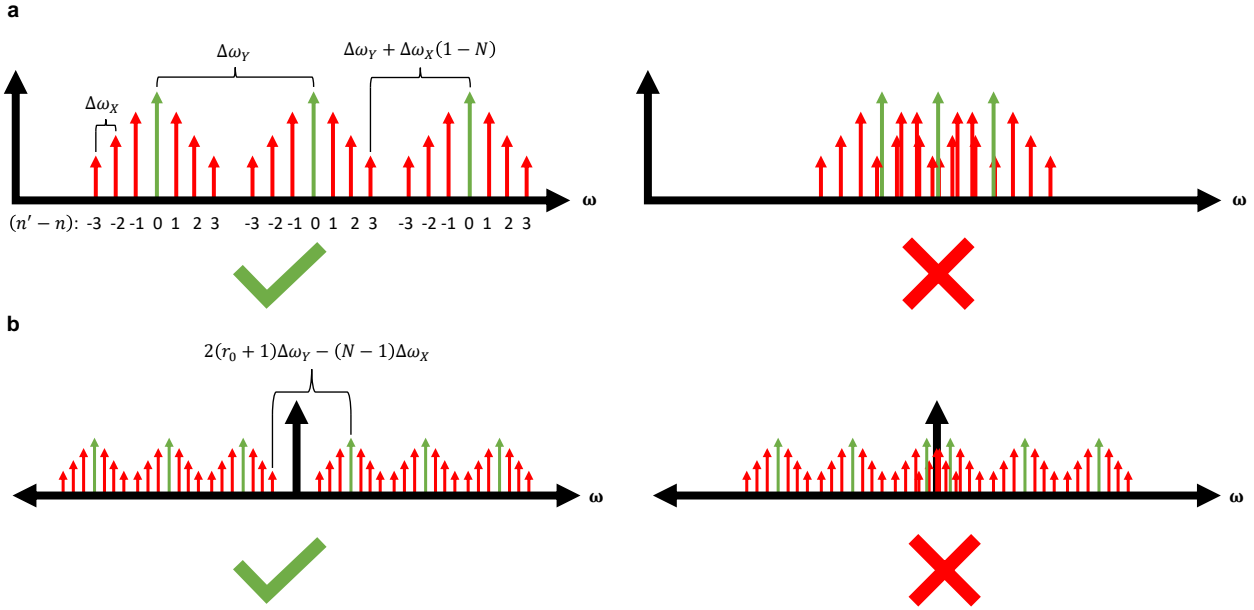


Figure 8. The anti-aliasing conditions for the frequency expansion scheme, where the output vector frequencies are green and the spurious frequencies are red. (a) The first type of aliasing comes from the spurious frequencies overlapping with the output vector frequencies. This can be avoided by increasing the output frequency spacing. (b) The second type of aliasing comes from the negative frequencies creeping up to the positive region. This can be avoided by increasing output frequency offset.

Now we can solve for the throughput in terms of the bandwidth, using the design choices mentioned in the anti-aliasing section, as those choices maximize the throughput. First, we can plug in the value of Δf_Y into the throughput equation using the anti-aliasing result $\Delta f_Y = \frac{1}{R}\Delta f_X$ to yield: $T_{\text{reduction}} = N \cdot \Delta f_X$.

Dividing the throughput by the bandwidth, we get:

$$\frac{T_{\text{reduction}}}{B} = \frac{N\Delta f_X}{N\Delta f_X + (r_0 + R)\Delta f_Y}.$$

Here, we can again plug in the anti-aliasing values of $\Delta f_Y = \frac{1}{R}\Delta f_X$ and $r_0\Delta f_Y = \frac{1}{2}(N - \frac{R+1}{R})\Delta f_X$, to yield:

$$\begin{aligned} \frac{N\Delta f_X}{N\Delta f_X + (r_0 + R)\Delta f_Y} &= \\ &= \frac{N\Delta f_X}{N\Delta f_X + \frac{1}{2}(N - \frac{R+1}{R})\Delta f_X + \frac{\Delta f_X}{\Delta f_Y}\Delta f_Y} \\ &= \frac{N\Delta f_X}{N\Delta f_X + \frac{1}{2}(N - \frac{R+1}{R})\Delta f_X + \Delta f_X} \\ &= \frac{N}{N + \frac{1}{2}(N - \frac{R+1}{R}) + 1} \\ &= \frac{2NR}{3NR + R + 1}, \end{aligned}$$

where the final equality came from simplifying the expression. To get the final approximation for the through-

put, we can take the reciprocal of this expression to see that:

$$\begin{aligned} \frac{B}{T_{\text{reduction}}} &= \frac{3NR + R + 1}{2NR} \\ &= \frac{3}{2} + \frac{1}{2N} - \frac{1}{2NR} \\ &\approx \frac{3}{2}, \quad \text{for } N \gg 1. \end{aligned}$$

Finally, taking the reciprocal again, we have both the exact and approximate expressions for the throughput of the frequency reduction scheme under the anti-aliasing conditions:

$$T_{\text{reduction}} = \frac{2NR}{3NR + R + 1}B \approx \frac{2}{3}B. \quad (7)$$

Next, we derive the throughput of the frequency expansion scheme under anti-aliasing conditions, which is a similar process. Returning to Equation 6, we must determine the limiting factor of the term $\min(\Delta f, f_0)$. In this case, the smallest frequency spacing in the signal will be Δf_X , since $\Delta f_Y > \Delta f_X$ for this scheme. And from the anti-aliasing analysis, the lowest frequency present in the output signal will be $(r_0 + 1)\Delta f_Y + (1 - N)\Delta f_X$.

When plugging in the design choices of $\Delta f_Y = N\Delta f_X$ and $r_0 = 0$, the lowest frequency present simply becomes Δf_X . Thus, the limiting factor of the term $\min(\Delta f, f_0)$ is Δf_X for the frequency expansion scheme.

Hence, the throughput becomes $T_{\text{expansion}} = N \cdot R \cdot \Delta f_X = R\Delta f_Y$, using the design choice above for the second equality. Dividing the throughput by the available bandwidth B , we get:

$$\begin{aligned} \frac{T_{\text{expansion}}}{B} &= \frac{R\Delta f_Y}{N\Delta f_X + (r_0 + R)\Delta f_Y} \\ &= \frac{R\Delta f_Y}{N\left(\frac{1}{N}\Delta f_Y\right) + (0 + R)\Delta f_Y} \\ &= \frac{R\Delta f_Y}{(1 + R)\Delta f_Y} \\ &= \frac{R}{1 + R} \\ &\approx 1, \quad \text{for } R \gg 1. \end{aligned}$$

Finally, the exact and approximate throughput of the frequency expansion scheme are:

$$T_{\text{expansion}} = \frac{R}{1 + R}B \approx B. \quad (8)$$

As discussed in the main text, if spurious frequencies are included as contributors to the throughput, then an multiplicative factor of N is added to Equation 6, which results in directly applying that same factor to Equations 7 and 8 for the spurious throughput. Note that in the main text, we assumed that the bandwidth B is available not only for the input and weight signals, but also for the output signal. So for the spurious throughput, all of the output spurious frequencies must fit within the bandwidth B . Fortunately, we see from Equation 4 that the highest spurious frequency is $(N - 1)\Delta f_X + (r_0 + R)\Delta f_Y$, which is less than B .

H. Non-WDM Throughput Derivation

Here we derive the throughput when not using optical WDM, meaning that it is limited to the electronic components. Thus, in this case, the bandwidth B is the bandwidth available from the DPMZMs, which was already derived in the previous section. The other constraint is the photodetector with bandwidth B_{PD} . The derivation for the throughput in terms of B_{PD} is similar to that for B , except that in this case, the maximum available bandwidth is determined by the highest output neuron frequency, which yields: $B_{PD} = (r_0 + R)\Delta f_Y$.

Starting with the frequency reduction scheme, we get:

$$\frac{T_{\text{reduction}}}{B_{PD}} = \frac{N\Delta f_X}{(r_0 + R)\Delta f_Y}.$$

Plugging in the anti-aliasing values of $\Delta f_Y = \frac{1}{R}\Delta f_X$ and $r_0\Delta f_Y = \frac{1}{2}(N - \frac{R+1}{R})\Delta f_X$ and simplifying, we get:

$$T_{\text{reduction}} = \frac{2NR}{NR + R - 1}B_{PD} \approx 2B_{PD}, \quad \text{for } N \gg 1$$

And for the frequency expansion scheme, we have:

$$\frac{T_{\text{expansion}}}{B_{PD}} = \frac{R\Delta f_Y}{(r_0 + R)\Delta f_Y}$$

Plugging in the anti-aliasing value $r_0 = 0$, we simply get:

$$T_{\text{expansion}} = B_{PD},$$

which is an exact value with no approximations.

Therefore for a given layer in the architecture, when limited to a modulation bandwidth of B and a single photodetector with bandwidth B_{PD} , the maximum throughput is:

$$T_{\text{reduction}} \approx \min\left(\frac{2}{3}B, 2B_{PD}\right) \quad (9)$$

$$T_{\text{expansion}} \approx \min(B, B_{PD}). \quad (10)$$

Additionally, Equations 9 and 10 show the relationship between the modulation bandwidth B (the highest frequency among the input and weight signals) and the photodetector bandwidth B_{PD} (the highest output neuron frequency). Equation 10 implies that for large R in the frequency expansion scheme, the maximum frequency contained among the input and weight signals is the same as the maximum frequency contained in the output neuron signal. This relation between B and B_{PD} can be confirmed by comparing their definitions, and supports the intuition that the electronics-limited throughput is simply the minimum of the modulator and photodetector bandwidths. And similarly for the frequency reduction scheme, Equation 9 implies that the maximum frequency among the input and weight signals is three times larger than that of the output neuron signal for large N .

I. DNN Random Partial Sum Training

Reading out the output vector after the photoelectric multiplication requires knowledge of the exact frequency content entering the system. Additionally, analog filters are required to isolate the output vector frequencies in both the frequency reduction and expansion schemes. However, in some applications it is desirable to have the flexibility to train a DNN anywhere in the spectrum without prior knowledge of the input, weight, and output frequencies.

Recall from Supplementary Section E that the spurious frequencies contain unique partial sums. Since these

| DNN Shape | Conventional Accuracy | MAFT-ONN Accuracy | MAFT-ONN Accuracy (Partial Sum Training) |
|---|-----------------------|-------------------|--|
| $7 \times 7 \rightarrow 32 \rightarrow 16 \rightarrow 10$ | 94.51% | 93.97% | 85.69% |
| $14 \times 14 \rightarrow 32 \rightarrow 16 \rightarrow 10$ | 95.12% | 95.98% | 86.45% |
| $28 \times 28 \rightarrow 1000 \rightarrow 1000 \rightarrow 10$ | 97.98% | 97.93% | 87.42% |
| $7 \times 7 \rightarrow 100 \rightarrow 100 \rightarrow 100 \rightarrow 100 \rightarrow 100 \rightarrow 100 \rightarrow 10$ | 97.05% | 95.80% | 93.52% |
| $28 \times 28 \rightarrow 100 \rightarrow 100 \rightarrow 100 \rightarrow 100 \rightarrow 100 \rightarrow 100 \rightarrow 10$ | 97.56% | 96.35% | 94.85% |

Table II. A comparison of the accuracy on the MNIST dataset on conventional DNNs with fully connected layers followed by a ReLU nonlinear activation versus simulations of the MAFT-ONN with the MZM nonlinear activation.

partial sums contain weight matrix elements, they too are trainable parameters for the DNN. Thus, assigning the output vector to random frequencies in the spectrum will result in training the DNN not with a conventional fully connected layer, but instead with a random assortment of partial sums. We call this method of DNN training *random partial sum training*.

We explored the effects of random partial sum training on larger DNNs using simulations, shown in Table II. The hardware setup in these simulations is different than in the 3-layer experiment. In the simulations, a bandpass filter is randomly placed in the spectrum within the general range of expected frequencies for each layer.

Table II compares the DNN accuracy between a conventional DNN using fully connected layers with each followed by a ReLU nonlinear activation, a simulation of the MAFT-ONN with fully connected layers followed by the MZM nonlinearity, and a simulation of the MAFT-ONN with bandpass filters placed randomly in the spectrum. As shown in Table II, the MAFT-ONN is on par with the accuracies of the conventional DNN. However, the random partial sum training version of the MAFT-ONN loses accuracy for smaller workloads, but begins to approach the performance of the conventional DNN for larger workloads. We hypothesize that the random partial sum training is less accurate because the density of partial sums in random places in the spectrum will be on average less than the density of partial sums at the output neuron values. But as the size and depth of the DNN

grows, the random partial sum training seems to converge to the conventional DNN accuracy, perhaps because the expressivity of the random partial sums increases.

In our 3-layer DNN experiment, we did not filter out the spurious frequencies after the first layer and randomly chose a set of output frequencies as the one-hot vectors for the MNIST classification. Thus, we experimentally demonstrated a variant of partial sum training.

J. Time-Multiplexed Matrix-Matrix Products

As mentioned in the main text, in addition to frequency-multiplexing, matrix-matrix products are also possible by time-multiplexing the input activation vectors. Figure 9 shows how the input matrix X is multiplexed in time-frequency space. The duration of each signal is $T = \frac{1}{\min(\Delta f, f_0)}$, where the input and weight signal must have the same duration T and be time-synchronized. (Note that this definition of T only applies to this section.) This time multiplexing does not change the throughput analysis, because the latency for each set of operations remains the same: latency = $\frac{1}{\min(\Delta f, f_0)}$.

Figure 9 also illustrates how the entire weight matrix is flattened in time to achieve the single-shot matrix-vector product at each time step. For a given layer of a DNN, the flattened weight matrix will be the same for each time step, creating an opportunity for energy efficient weight reuse through optical fan-out and time delay lines.

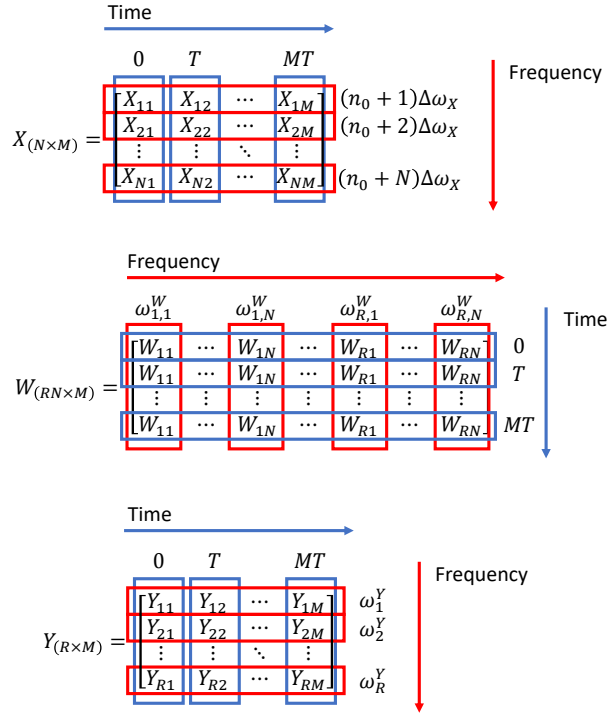


Figure 9. A visualization of the matrix-matrix product in time-frequency space. At each time step, a new input vector is multiplied to the same weight matrix. The weight matrix is flattened to fit within a single time step for the single-shot matrix-vector product in the frequency domain.